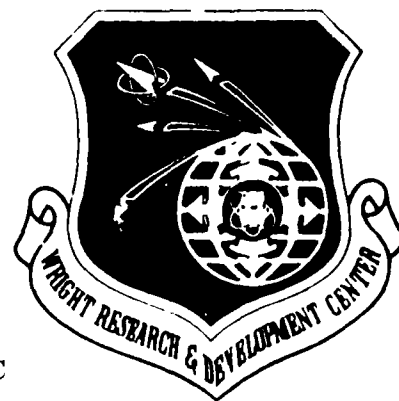


2

WRDC-TR-90-3076

AD-A232 405



**COMPUTATION OF VISCOUS SHOCK/SHOCK HYPERSONIC
INTERACTIONS WITH AN IMPLICIT FLUX SPLIT SCHEME**

Datta Gaitonde
Universal Energy Systems
4401 Dayton-Xenia Road
Dayton, OH 45432

December 1990

Final Report for Period September 1989 - September 1990

Approved for public release; distribution unlimited.

DTIC
ELECTE
MAR 6 1991
S B D

**FLIGHT DYNAMICS LABORATORY
WRIGHT LABORATORY
AIR FORCE SYSTEMS COMMAND
WRIGHT-PATTERSON AIR FORCE BASE, OHIO 45433-6553**


91 3 04 043

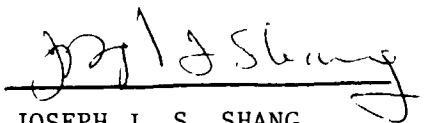
NOTICE

WHEN GOVERNMENT DRAWINGS, SPECIFICATIONS, OR OTHER DATA ARE USED FOR ANY PURPOSE OTHER THAN IN CONNECTION WITH A DEFINITELY GOVERNMENT-RELATED PROCUREMENT, THE UNITED STATES GOVERNMENT INCURS NO RESPONSIBILITY OR ANY OBLIGATION WHATSOEVER. THE FACT THAT THE GOVERNMENT MAY HAVE FORMULATED OR IN ANY WAY SUPPLIED THE SAID DRAWINGS, SPECIFICATIONS, OR OTHER DATA, IS NOT TO BE REGARDED BY IMPLICATION, OR OTHERWISE IN ANY MANNER CONSTRUED, AS LICENSING THE HOLDER, OR ANY OTHER PERSON OR CORPORATION; OR AS CONVEYING ANY RIGHTS OR PERMISSION TO MANUFACTURE, USE, OR SELL ANY PATENTED INVENTION THAT MAY IN ANY WAY BE RELATED THERETO.

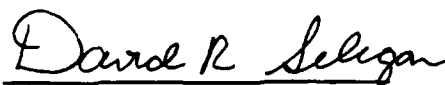
THIS REPORT IS RELEASABLE TO THE NATIONAL TECHNICAL INFORMATION SERVICE (NTIS). AT NTIS IT WILL BE AVAILABLE TO THE GENERAL PUBLIC, INCLUDING FOREIGN NATIONS.

THIS TECHNICAL REPORT HAS BEEN REVIEWED AND IS APPROVED FOR PUBLICATION.


DATTa GAITONDE
Visiting Scientist


JOSEPH J. S. SHANG
Technical Manager
Computational Aerodynamics

FOR THE COMMANDER


DAVID R. SELEGAN
Actg Chief
Aeromechanics Division

IF YOUR ADDRESS HAS CHANGED, IF YOU WISH TO BE REMOVED FROM OUR MAILING LIST, OR IF THE ADDRESSEE IS NO LONGER EMPLOYED BY YOUR ORGANIZATION PLEASE NOTIFY WL/FIMM, WRIGHT-PATTERSON AFB, OH 45433-6553 TO HELP MAINTAIN A CURRENT MAILING LIST.

COPIES OF THIS REPORT SHOULD NOT BE RETURNED UNLESS RETURN IS REQUIRED BY SECURITY CONSIDERATIONS, CONTRACTUAL OBLIGATIONS, OR NOTICE ON A SPECIFIC DOCUMENT.

REPORT DOCUMENTATION PAGE			Form Approved OMB No 0704-0188	
<small>Public reporting burden for this collection of information is estimated to average 1 hour per response, including the time for reviewing instructions, searching existing data sources, gathering and maintaining the data needed, and completing and reviewing the collection of information. Send comments regarding this burden estimate or any other aspect of this collection of information, including suggestions for reducing this burden, to Washington Headquarters Services, Directorate for Information Operations and Reports, 1215 Jefferson Davis Highway, Suite 1204, Arlington, VA 22202-4302, and to the Office of Management and Budget, Paperwork Reduction Project (0704-0188), Washington, DC 20503.</small>				
1. AGENCY USE ONLY (Leave blank)	2. REPORT DATE December 1990	3. REPORT TYPE AND DATES COVERED Final Report 7 Sep 89 to 7 Sep 90		
4. TITLE AND SUBTITLE Computation of Viscous Shock/Shock Hypersonic Interactions with an Implicit Flux Split Scheme		5. FUNDING NUMBERS C-F33615-88-C-2908 ZE-61102F PR-2307 TA-N6 WU-11		
6. AUTHOR(S) Datta Gaitonde				
7. PERFORMING ORGANIZATION NAME(S) AND ADDRESS(ES) Universal Energy Systems 4401 Dayton-Xenia Road Dayton OH 45433-1894		8. PERFORMING ORGANIZATION REPORT NUMBER		
9. SPONSORING / MONITORING AGENCY NAME(S) AND ADDRESS(ES) Flight Dynamics Laboratory WL/FIMM, (Dr. Joseph Shang, 255-2455) Wright-Patterson AFB OH 45433-6553		10. SPONSORING / MONITORING AGENCY REPORT NUMBER WRDC-TR-90-3076		
11. SUPPLEMENTARY NOTES				
12a. DISTRIBUTION / AVAILABILITY STATEMENT Approved for public release; distribution is unlimited			12b. DISTRIBUTION CODE	
13. ABSTRACT (Maximum 200 words) The interaction of an impinging shock with the bow-shock generated by a blunt geometry is examined numerically for hypersonic (Mach 8, perfect gas) flows with modified Steger-Warming flux-split scheme. The modifications are designed to reduce numerical dissipation in the boundary layer thus improving the resolution and accuracy of the resulting algorithm. The full 2-D Navier-Stokes equations are solved in finite-volume formulation with central differencing for viscous terms and residual driven line Gauss-Seidel relaxation for time advancement. Grid resolution studies are performed. For a Type IV interaction, comparison with surface pressure and heat-transfer rates display good overall agreement with experimental values. For a Type III ⁺ interaction, a detailed comparison is made with experimental surface quantities and a computation with Van Leer's flux-splitting algorithm. The peak amplification of pressure is modestly over-predicted with the current algorithm. The computed peak heat transfer is comparable to that obtained in previous research with Van Leer's splitting, although anomalous behavior is observed in the vicinity of the stagnation point. This behavior may be eliminated with appropriate corrections.				
14. SUBJECT TERMS Shock-on-Shock Interaction, Hypersonic, Numerical Flux/Split			15. NUMBER OF PAGES 54	
			16. PRICE CODE	
17. SECURITY CLASSIFICATION OF REPORT Unclassified	18. SECURITY CLASSIFICATION OF THIS PAGE Unclassified	19. SECURITY CLASSIFICATION OF ABSTRACT Unclassified	20. LIMITATION OF ABSTRACT	

GENERAL INSTRUCTIONS FOR COMPLETING SF 298

The Report Documentation Page (RDP) is used in announcing and cataloging reports. It is important that this information be consistent with the rest of the report, particularly the cover and title page. Instructions for filling in each block of the form follow. It is important to *stay within the lines* to meet *optical scanning requirements*.

Block 1. Agency Use Only (Leave blank).

Block 2. Report Date. Full publication date including day, month, and year, if available (e.g. 1 Jan 88). Must cite at least the year.

Block 3. Type of Report and Dates Covered. State whether report is interim, final, etc. If applicable, enter inclusive report dates (e.g. 10 Jun 87 - 30 Jun 88).

Block 4. Title and Subtitle. A title is taken from the part of the report that provides the most meaningful and complete information. When a report is prepared in more than one volume, repeat the primary title, add volume number, and include subtitle for the specific volume. On classified documents enter the title classification in parentheses.

Block 5. Funding Numbers. To include contract and grant numbers; may include program element number(s), project number(s), task number(s), and work unit number(s). Use the following labels:

C - Contract	PR - Project
G - Grant	TA - Task
PE - Program Element	WU - Work Unit Accession No.

Block 6. Author(s). Name(s) of person(s) responsible for writing the report, performing the research, or credited with the content of the report. If editor or compiler, this should follow the name(s).

Block 7. Performing Organization Name(s) and Address(es). Self-explanatory.

Block 8. Performing Organization Report Number. Enter the unique alphanumeric report number(s) assigned by the organization performing the report.

Block 9. Sponsoring/Monitoring Agency Name(s) and Address(es). Self-explanatory.

Block 10. Sponsoring/Monitoring Agency Report Number. (If known)

Block 11. Supplementary Notes. Enter information not included elsewhere such as: Prepared in cooperation with ...; Trans. of ...; To be published in ... When a report is revised, include a statement whether the new report supersedes or supplements the older report.

Block 12a. Distribution/Availability Statement. Denotes public availability or limitations. Cite any availability to the public. Enter additional limitations or special markings in all capitals (e.g. NOFORN, REL, ITAR).

DOD - See DoDD 5230.24, "Distribution Statements on Technical Documents."

DOE - See authorities.

NASA - See Handbook NHB 2200.2.

NTIS - Leave blank.

Block 12b. Distribution Code.

DOD - Leave blank.

DOE - Enter DOE distribution categories from the Standard Distribution for Unclassified Scientific and Technical Reports.

NASA - Leave blank.

NTIS - Leave blank.

Block 13. Abstract. Include a brief (*Maximum 200 words*) factual summary of the most significant information contained in the report.

Block 14. Subject Terms. Keywords or phrases identifying major subjects in the report.

Block 15. Number of Pages. Enter the total number of pages.

Block 16. Price Code. Enter appropriate price code (*NTIS only*)

Blocks 17. - 19. Security Classifications. Self-explanatory. Enter U.S. Security Classification in accordance with U.S. Security Regulations (i.e., UNCLASSIFIED). If form contains classified information, stamp classification on the top and bottom of the page.

Block 20. Limitation of Abstract. This block must be completed to assign a limitation to the abstract. Enter either UL (*unlimited*) or SAR (*same as report*). An entry in this block is necessary if the abstract is to be limited. If blank, the abstract is assumed to be unlimited.

Contents

List of Figures	iv
List of Tables	v
Acknowledgements	vi
1 Introduction	1
2 Objective	7
3 Theoretical Model	9
4 Classification of Computations	15
5 Boundary Conditions and Numerical Details	20
6 Results and Discussion	22
6.1 Configuration A	22
6.2 Configuration B	25
7 Conclusions	47
8 References	48
Nomenclature	52



Accession For	
NTIS GRA&I	<input checked="" type="checkbox"/>
DTIC TAB	<input type="checkbox"/>
Unannounced	<input type="checkbox"/>
Justification	
By	
Distribution/	
Availability Codes	
Dist	Avail and/or Special
A-1	

List of Figures

1.1	Schematic of NASP vehicle. From [2]	5
1.2	Type <i>III</i> and <i>IV</i> shock interference patterns. From [7]	6
4.1	Geometry and boundary conditions	18
4.2	Grids for Configs. A and B	19
6.1	Surface heat-transfer comparison - Config. A	31
6.2	Surface pressure comparison - Config. A	31
6.3	Effect of grid resolution - Config. A	32
6.4	Comparison of pressure contours - Config. A	33
6.5	Comparison of Mach contours - Config. A	35
6.6	Streamlines - Config. A (Grid A3)	37
6.7	Sonic line - Config. A (Grid A3)	38
6.8	Comparison of surface pressure - Config. B	39
6.9	Comparison of surface heat-transfer - Config. B	40
6.10	Location of pressure and heat-transfer peaks - Config. B2	41
6.11	Corrected surface heat-transfer - Config. B2	42
6.12	Comparison of pressure contours - Config. B	43
6.13	Comparison of Mach contours - Config. B	44
6.14	Sonic Line - Config. B2	45
6.15	Streamline comparison - Config. B	46

List of Tables

4.1	Flow parameters	16
4.2	Grid details	17
6.1	Peak pressure and heat-transfer values - Config. A	24
6.2	Peak pressure and heat-transfer values - Config. B	27

Acknowledgements

The author wishes to thank Dr. Joseph Shang for his constant support and encouragement and Prof. MacCormack of Stanford University for several insightful discussions. The computations were performed on computers at WPAFB and the NAS program. The assistance of the staff at both locations is gratefully acknowledged.

1. Introduction

Viscous shock-on-shock interactions occur on typical aerospace configurations such as the proposed NASP vehicle and the space shuttle. The forebodies of proposed hypersonic aircraft (Fig. 1.1) form ramp-like structures designed to compress the incoming air with oblique shocks and therefore act as the compressor system for the inlet. For optimum mass flow through the inlet, these compression system shocks, which may form a relatively strong oblique shock in conjunction with the vehicle bow shock, should be positioned to converge on the inlet cowl leading edge [1] where they interact with the bow shock produced by the cowl lip. Viscous hypersonic shock-on-shock interactions (often denoted "interfering" flows) can significantly affect the performance of the inlet through the creation of anomalous pressure and heat transfer peaks on the cowl leading edge.

The ability to accurately and efficiently predict flow characteristics of interfering flows is critical for successful design [2]. This effort has therefore received significant impetus in recent years under the auspices of the NASP Project. A recent report, *Hypersonic Technology for Military Applications* [3], emphasizes the importance of the study of such interactions:

The most intense local heating rates on vehicles such as the projected NASP research vehicle are expected to be on cowl lips, caused by shock-on-shock heating.

Edney [4] classified shock interference patterns into six types. The actual pattern established in a particular case depends primarily upon the strength and location of the impinging shock, the characteristics of the incoming flow and the cowl shape. Efforts at understanding interfering flows have focused on experimental [4, 5, 6, 7], semiempirical [8], theoretical [9, 10] and, in recent years, numerical simulations [1, 2, 11, 12, 13].

Most studies so far have focused on Type *III* and Type *IV* interactions which result in the highest mechanical and thermal loading on the cowl lip (Fig. 1.2). These types of interactions occur when the impinging shock intersects the subsonic portion of the cowl bow shock — the cowl

is typically replaced by a cylinder to simplify analysis. A supersonic viscous shear layer emanates from the point of impingement and, depending upon the angle between the shear layer and the surface tangent at the point where the shear layer hits the surface, this layer either merges with the boundary layers where it strikes the body and becomes an attached subsonic layer (Type *III*) or, the shear layer forms a "jet" which strikes the body after the formation of a terminating jet bow shock (Type *IV*) [1, 10]. The process of jet impingement (Type *IV*) results in maximum augmentation of peak heat-transfer and surface pressure.

Initial theoretical/numerical efforts, relied upon semiempirical approaches requiring specification of several parameters such as shock standoff distance. Hains and Keyes [14], for example, utilized several assumptions to develop empirical correlations for peak heat transfer amplification. Based on a study of flow past simple body shapes at different Mach numbers (6.0 and 20.2) and specific heat ratios (1.2 to 1.6), they concluded that effect of an impinging shock is most drastic for Type *IV* interactions with amplification up to 17 times (over the noninterfering case) for heat-transfer rate and 8 times for peak pressure. Other notable efforts include the work of Crawford [9] who developed a graphical method of pattern prediction and Bramlette [10] who introduced further simplifications to Crawford's method.

The advent of more sophisticated methods and high-speed computers saw significant advances in the use of computational methods. Tannehill *et al.* [11] solved the full 2-D Navier-Stokes equations with shock capturing as well as shock fitting methods for low and high Reynolds Numbers respectively for Type *III* and *IV* flows around a cylinder at Mach 4.6. Although their explicit algorithm suffered significant step size limitations, they successfully validated their approach by comparison with the results of Beckwith and Cohen [15] and Edney [4]. White and Rhie [1] computed blunt cowl flows with (Mach 6) and without (Mach 15) shock impingement with a pressure based implicit finite volume scheme. Their results compared well with the experiments of Craig and Ortwerth [6] and Tannehill *et al.* [11].

The complexity of the wave structure of shock-on-shock interactions of the type investigated

in this research all but obviates the use of shock-fitting methods. Modern analyses utilize shock capturing methods almost exclusively. The first few popular shock-capturing schemes such as the centered MacCormack scheme [16] utilized by Tannehill *et al* or the Jameson scheme [17] require the addition of explicit damping terms to avoid overshoots and oscillations leading often to extremely smeared shocks for hypersonic flows.

The underlying philosophy of more recent shock-capturing methods is either mathematical (for example TVD schemes [18]) or physical (for example flux-splitting [19, 20]). Many modern schemes employ upwinding to obtain algorithms possessing better dissipation characteristics, higher stability bounds and increased numerical efficiency [21, 22]. A brief description of modern schemes utilized in the recent past for the types of flows under investigation is presented below.

TVD schemes, upwind biased and symmetric, have gained rapid popularity in recent years [23] and have been applied for several flows including shock wave diffraction, flows past airfoils, complex vehicle shapes [24], boundary layers and shock boundary layer interactions [25]. Klopfer and Yee [2] computed noninterfering and interfering patterns of all types identified by Edney [4] for Mach 6, 8 and 15 flows. Utilizing the thin-layer Navier Stokes equations, they suggested grid resolution criteria for noninterfering flows and concluded that their scheme performed relatively well for 2-D flows though modest discrepancies existed in comparison with experimental heat transfer data.

The popular van Leer [20] and Steger-Warming [19] flux-split schemes have been applied to several inviscid and viscous flows in explicit and implicit formulations. Applications with van Leer's scheme include inviscid subsonic and transonic flows over airfoils [26], viscous shock-induced separated flows [27] and flows over delta wings [28]. Recently, Moon and Holt [12] reported a computation with van Leer splitting for inviscid fluxes and a centered scheme for viscous terms for a Type *III*⁺ interaction (Mach 8) with and without a turbulence model. Their results indicate significant overprediction of surface peak pressures for the laminar case and underprediction of peak heat transfer for both cases. In addition, the turbulent computation displays spatial oscillations

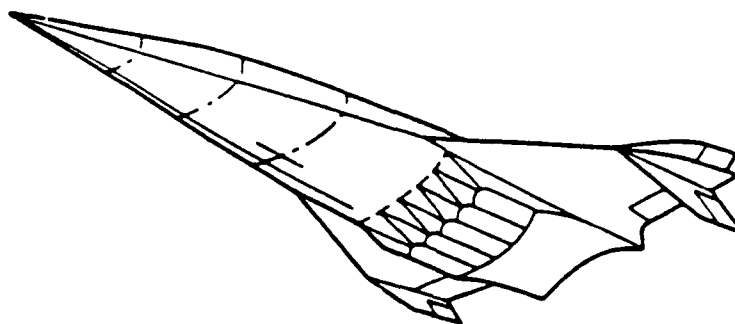
in the region of maximum heat transfer.

Reported applications of the Steger-Warming algorithm include inviscid flows past airfoils [19] and cylinders [29]. The numerical algorithm employed in the current effort is a modified Steger-Warming scheme proposed by MacCormack and Candler [30] (Section 3). This scheme has previously been applied for flat plate boundary layer flows, flows past compression ramps, blunt body flows [30] and for viscous real gas flows past sphere-cones [31]. A comparison of the van Leer and the original Steger-Warming scheme for some Euler flows may be found in Anderson *et al.* [32].

Recent research in the computation of hypersonic flows has also focused on unstructured grid methods which are typically well-suited to adaptive techniques. Thareja *et al.* [13] presented a 2-D upwind finite element technique using cell centered quantities and implicit and/or explicit time marching with adaptive unstructured triangular grids. They implemented a first order basic and a higher order flux corrected scheme [33] with an essentially point Gauss-Seidel implicit algorithm. The shocks obtained with this method are crisp though some smear is evident in the shear layers. Surface quantities including pressure and heat transfer rates compare very well with other computational schemes and experimental data.

This report first outlines the objectives of this research effort. This is followed by a relatively detailed exposition of the numerical algorithm in so far as the inviscid flux evaluation is concerned. For the purposes of brevity, the Gauss-Seidel line relaxation algorithm employed for time advancement is only summarized. The computations described are then classified prior to the discussion of the results.

TYPICAL CONFIGURATION



TYPICAL OVERALL FLOW FIELD

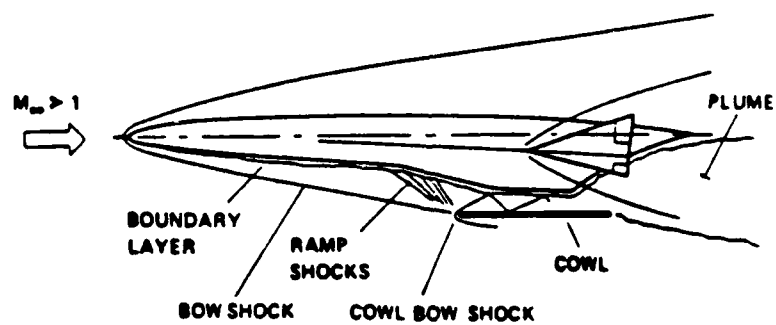
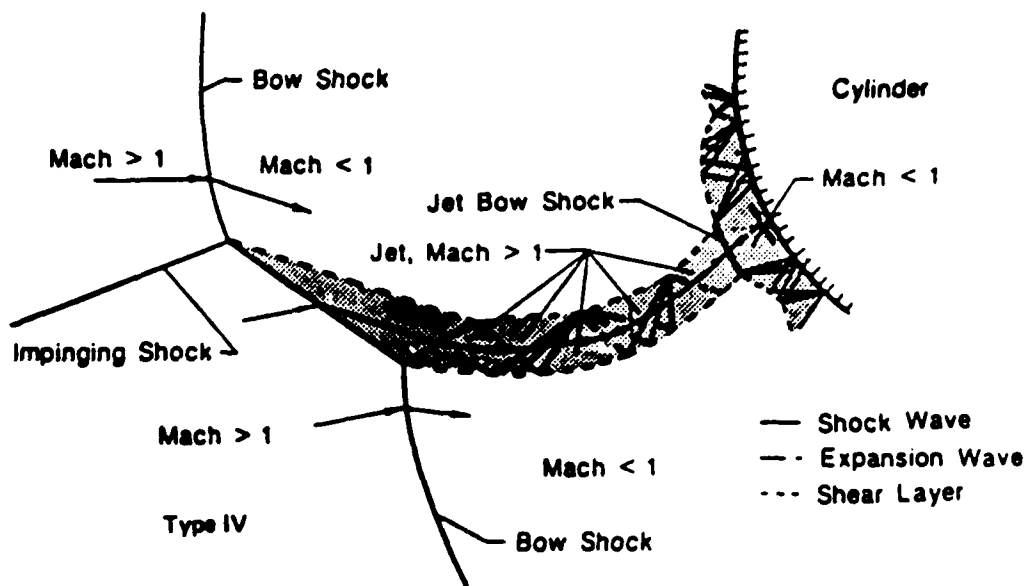


Figure 1.1: Schematic of NASP vehicle. From [2]



6

2. Objective

The computation of shock-on-shock interactions is a challenging task requiring the resolution of intense shock waves and slip streams and their interactions with each other and the boundary layer. As mentioned earlier, interfering viscous hypersonic flows past cylinders have been computed previously with TVD schemes [2], van Leer splitting [12] and finite element flux corrected transport methods [13]. Each of these methods possesses some degree of built in or explicitly added damping to stabilize the calculation in regions of high gradients such as shock waves. A brief description of the damping properties of several popular schemes is presented in Ref. [34]. Several modern schemes were in fact developed primarily to handle inviscid dominated phenomena and focused almost exclusively on wave propagation by considering only the inviscid terms in the governing equations. The introduction of viscous terms (typically through central differencing) introduces contradictory requirements on the numerical scheme i.e., shock-capturing requires a finite amount of numerical dissipation which must not however, overwhelm the physical dissipation in the boundary layer.

The fundamental objective of this study is to utilize the modified Steger-Warming flux split scheme of MacCormack and Candler [30] to examine viscous shock-on-shock impingement flow-fields. A salient objective is to examine the characteristics of the scheme with grid resolution studies and to compare this scheme with others. The choice of scheme is motivated by the following factors. 1) The modifications specifically address the issue of excessive dissipation in the boundary layer. Such undesirable dissipation can significantly degrade the evaluation of surface quantities. 2) The algorithm has been extended to include non-equilibrium real gas and successfully applied for hypersonic blunt body flows [35]. It is an attractive candidate for further work on complex hypersonic 3-D configurations and thus, its capabilities and limitations warrant further investigation especially under complex flow conditions.

The configurations examined in this paper are necessarily dictated by the availability of ex-

isting experimental and numerical investigations. For the purposes of comparison with other schemes, the computations of Moon and Holt [12] (Type III^+) and Thareja *et al.* [13] (Type IV) are utilized as described later.

3. Theoretical Model

The 2-D Navier Stokes equations in strong conservation form are solved in the transformed (ξ, η) coordinates:

$$\frac{\partial \bar{U}}{\partial t} + \frac{\partial \bar{F}}{\partial \xi} + \frac{\partial \bar{G}}{\partial \eta} = 0 \quad (3.1)$$

where \bar{U} , \bar{F} and \bar{G} are vectors as defined below and $\xi(x, y)$ and $\eta(x, y)$ are the transformed variables (with $\partial \xi / \partial x$ denoted by ξ_x , etc.). The solution vector \bar{U} is written as:

$$\bar{U} = \frac{1}{J} \begin{pmatrix} \rho \\ \rho u \\ \rho v \\ \rho e \end{pmatrix}, \quad (3.2)$$

and the flux vectors \bar{F} and \bar{G} are:

$$\bar{F} = \frac{1}{J} \begin{pmatrix} \rho U \\ \rho u U + \xi_x(p - \tau_{xx}) - \xi_y \tau_{xy} \\ \rho v U + \xi_y(p - \tau_{yy}) - \xi_x \tau_{xy} \\ (\rho e + p)U + \xi_x \beta_x - \xi_y \beta_y \end{pmatrix}, \quad (3.3)$$

$$\bar{G} = \frac{1}{J} \begin{pmatrix} \rho V \\ \rho u V + \eta_x(p - \tau_{xx}) - \eta_y \tau_{xy} \\ \rho v V + \eta_y(p - \tau_{yy}) - \eta_x \tau_{xy} \\ (\rho e + p)V + \eta_x \beta_x - \eta_y \beta_y \end{pmatrix}, \quad (3.4)$$

and, in Eqns. 3.3 and 3.4, the contravariant velocity vectors U and V are:

$$U = \xi_x u + \xi_y v \quad (3.5)$$

$$V = \eta_x u + \eta_y v \quad (3.6)$$

and J is the Jacobian of the transformation, with subscripts indicating derivatives ($\xi_x \equiv \partial\xi/\partial x$):

$$J^{-1} = x_\xi y_\eta - x_\eta y_\xi \quad (3.7)$$

The components of the Cartesian stress tensor $\bar{\tau}$ may be written as,

$$\tau_{xx} = \lambda \nabla \cdot \vec{v} + 2\mu \frac{\partial u}{\partial x} \quad (3.8)$$

$$\tau_{xy} = \mu \left(\frac{\partial u}{\partial y} + \frac{\partial v}{\partial x} \right) \quad (3.9)$$

$$\tau_{yy} = \lambda \nabla \cdot \vec{v} + 2\mu \frac{\partial v}{\partial y} \quad (3.10)$$

where $\lambda = -2/3\mu$, and

$$\beta_x = Q_x - u\tau_{xx} - v\tau_{xy} \quad (3.11)$$

$$\beta_y = Q_y - u\tau_{xy} - v\tau_{yy} \quad (3.12)$$

The components of the heat flux vector are

$$Q_x = -\gamma \frac{\mu}{Pr} \frac{\partial e_i}{\partial x} \quad (3.13)$$

$$Q_y = -\gamma \frac{\mu}{Pr} \frac{\partial e_i}{\partial y} \quad (3.14)$$

The Cartesian velocity components in the (x, y) coordinates are denoted by (u, v) . For the configurations under consideration, the η coordinate lines are in the generally radial direction while the ξ lines are circumferential. The density ρ , static pressure p and static temperature T are related through the equation of state $p = \rho RT$ where R is the gas constant. The total energy per unit mass is given by $e = e_i + 0.5(u^2 + v^2 + w^2)$, where the internal energy per unit mass e_i is equal to $C_v T$. The molecular dynamic viscosity μ is given by the Sutherland's law:

$$\mu = C_1 \frac{T_2^{\frac{3}{2}}}{T + C_2} \quad (3.15)$$

where C_1 and C_2 are constants ($= 1.45 \times 10^{-6} kg/(m \ s\sqrt{K})$ and $110.4K$ respectively). The molecular Prandtl number $Pr = C_p \mu / k$ is taken to be 0.73 (air).

The above equations are solved in discretized form with the cell-centered finite volume Gauss-Seidel line relaxation numerical algorithm described in [36] utilizing the approach described in [30] to evaluate the inviscid fluxes. A brief development of the algorithm is presented for completeness with reference to the evaluation of the flux at the cell surface $j + \frac{1}{2}$. The flux computation proceeds separately for the viscous and inviscid parts. At any time level, suppressing the overbars,

$$G_{j+\frac{1}{2}} = G_{I,j+\frac{1}{2}} + G_{V,j+\frac{1}{2}} \quad (3.16)$$

where the subscripts I and V denote the inviscid and viscous components respectively. Since the inviscid fluxes are homogeneous, following the procedure of Steger and Warming [19], they may be split into subvectors possessing advantageous eigenvalue properties:

$$G_I^n = B^n \bar{U}^n = (B_+^n + B_-^n) \bar{U}^n \quad (3.17)$$

Utilizing the hyperbolic nature of the inviscid fluxes, the Jacobian B is diagonalized with a similarity transformation:

$$B = Q^{-1} \Lambda Q = Q^{-1} (\Lambda^+ + \Lambda^-) Q = \bar{B}_+ + \bar{B}_- \quad (3.18)$$

where Λ is a diagonal matrix consisting of the eigenvalues of B and Λ^+ and Λ^- denote the splitting of the eigenvalues into positive and negative components. For simplicity of evaluation, Q may further be written as:

$$Q = CRS \quad (3.19)$$

where R is a rotation matrix, $S = \frac{\partial V}{\partial U}$, V is the vector of non-conserved variables $\{\rho, u, v, p\}$ and C diagonalizes the flux vector G written in terms of V . At a face $j + 1/2$ therefore, the flux according to the method of Steger and Warming may be written as:

$$G_{I,j+\frac{1}{2}} = B_{+,j} \bar{U}_{i,j} + B_{-,j+1} \bar{U}_{i,j+1} \quad (3.20)$$

The quantities \bar{U} are obtained at the cell interfaces by extrapolating the conserved variables to the cell surface with the MUSCL approach of Anderson *et al.* [32] as described below. The formula

of Eqn. 3.20 exhibits two major difficulties. First, it may introduce discontinuities in the solution at sonic and stagnation points where the eigenvalues change sign and some form of eigenvalue smoothing may be necessary. For one of the computations reported in this report, smoothing proportional to the eigenvalue gradients (cf. [32]) is employed (Section 6.2). A more serious problem introduced by the evaluation of Eqn. 3.20 is the problem of excessive numerical damping introduced in the boundary layers. This damping significantly deteriorates the evaluation of surface quantities of engineering interest. MacCormack and Candler [30] considered the determination of the normal flux near a surface under boundary layer conditions. With direct algebraic manipulation, they proved that the Steger Warming procedure introduces artificial tangential momentum exchange between adjacent cells in the boundary layer solely due to the splitting of the inviscid fluxes. This diffusive term is proportional to the quantity:

$$\frac{c}{2\gamma} \rho_{i,j} (u_{i,j+1} - u_{i,j}) \quad (3.21)$$

Since it is of order Δy , it can obtain unacceptably high values in the boundary layer. In addition, there is also a large numerical exchange of kinetic energy of the order:

$$\frac{c}{2\gamma} \rho_{i,j} (\alpha_{i,j+1} - \alpha_{i,j}) \quad (3.22)$$

between adjacent points in the boundary layer where α is the kinetic energy. They recommended that both $B_{+,j+\frac{1}{2}}$ and $B_{-,j+\frac{1}{2}}$ be evaluated at the *same* point (either j or $j+1$). In the present calculations, following this recommendation:

$$j + \frac{1}{2} = \begin{cases} j, & n \text{ odd} \\ j+1, & n \text{ even} \end{cases} \quad (3.23)$$

where n is the current iteration number. Further investigation showed however, that this modification introduced a second order fictitious pressure gradient across the boundary layer. This error comprised the terms:

$$\frac{\gamma-1}{2} \rho_{i,j} \left[(u_{i,j+\frac{1}{2}} - u_{i,j})^2 + (v_{i,j+\frac{1}{2}} - v_{i,j})^2 \right] \quad (3.24)$$

and may therefore be expected to dominate only in the close vicinity of the boundary where high velocity gradients exist. MacCormack and Candler corrected this gradient at the expense of reintroducing some of the diffusiveness of the Steger Warming scheme by further modifying the component S for the matrix Q in Eqn. 3.19 so that its last row is evaluated as in the original formulation. In this work, this *last row* (LR) correction is applied in a linear fashion starting at the nominal edge of the boundary layer obtaining the full correction at the surface.

The modifications described above were developed for application only in the boundary layers and in fact lead to instability when applied in regions of discontinuities such as shock waves. As a result, it is necessary to revert to the original Steger Warming scheme near shocks. Further, in order to retain the monotonic nature of the solution, it is also necessary to revert to first order accuracy at such regions. The order of the solution is determined by appropriate extrapolation of the conserved variables as in the MUSCL approach which is known to be superior to the flux-differencing approach in which the split fluxes are first evaluated at the nodal points and then extrapolated to the cell surfaces [32].

$$\bar{U}_{j+\frac{1}{2}}^- = \bar{U}_j + \phi_j^- \frac{(\bar{U}_j - \bar{U}_{j-1})}{2} \quad (3.25)$$

$$\bar{U}_{j+\frac{1}{2}}^+ = \bar{U}_{j+1} - \phi_{j+1}^+ \frac{(\bar{U}_{j+2} - \bar{U}_{j+1})}{2} \quad (3.26)$$

where the superscripts $-$ and $+$ indicate states to the left and right respectively of the interface $j + \frac{1}{2}$.

Formal first and second order accuracy is obtained by choosing the term ϕ^\pm equal to zero and one respectively. A pressure switch given by (for the $j + \frac{1}{2}$ face):

$$\phi_j^- = \begin{cases} 0 & \text{if } \left| \frac{P_j - P_{j-1}}{\min\{P_j, P_{j-1}\}} \right| \geq \Delta \\ 1 & \text{otherwise} \end{cases} \quad (3.27)$$

is utilized to determine regions where the scheme must revert to the first order accurate Steger

Warming method for monotonicity and stability. The value of Δ is typically fixed at 0.25. Other strategies are described in [23, 32].

The governing equations (Eqn. 3.1) are integrated with a residual driven line Gauss-Seidel relaxation scheme as described in the works of MacCormack [36] and Candler [35]. With first-order backward Euler time discretization and linearization of the fluxes in time, the discretized equation may be written in the form:

$$\{NUMERICS\} \delta \bar{U} = PHYSICS \quad (3.28)$$

where *PHYSICS* represents the residual and *NUMERICS* contains the driving terms and $\delta \bar{U}$ represents the change in the solution vector at each time step. The full Navier-Stokes equations are utilized in computing the residual. The viscous terms in the residual are evaluated with the second order (in space and time) predictor-corrector algorithm of MacCormack[16]. One advantage of the above methodology is that since the *NUMERICS* portion of the code is simply a driver for the solution, approximations may be utilized. In fact, Liou and van Leer [37] point out that even if the *PHYSICS* term is evaluated with other methods (such as van Leer's splitting or Roe's upwinding), the use of Steger Warming splitting in evaluating the *NUMERICS* portion leads to robust codes for the Newton linearization procedure. In this research, the viscous Jacobians in the driving *NUMERICS* portion are computed with the thin layer approximation.

When solved with the Gauss-Seidel line relaxation procedure, Eqn. 3.28 represents a block tridiagonal system displaying strong diagonal dominance when the above flux-splitting is employed. For transonic and supersonic flows, line relaxation methods are superior to approximate factorization methods in convergence rate which amply compensates for the larger computation required per iteration [38]. The line Gauss-Seidel algorithm is also unconditionally stable in the linear analysis and is known to be relatively insensitive to the choice of time increment per iteration.

4. Classification of Computations

The geometrical complexity of a 3-D cowl is separated from the physics of the flow features by considering a simplified geometry as shown schematically in Fig 4.1. The cowl is replaced by a cylinder in an oncoming flow containing the impinging shock. The length dimensions and flow parameters chosen (described below) are determined by availability of experimental data and existing numerical studies for comparison purposes. The characteristics of the impinging shock are uniquely specified by the flow deflection angle and a reference point in the oncoming flow. Two distinct configurations are computed with the main distinction being in the shock strength and impingement location.

The first set of computations corresponds to the experimental configuration of Wieting and Holden [5] and computed with an adaptive upwind finite element technique by Thareja *et al.* [13]. This configuration, representing the computation described in most detail by Thareja *et al.*, will be denoted henceforth as Config. A. The second set of computations, denoted Config. B is based on the experiments of Wieting [39] and computed with the van Leer flux-split scheme by Moon and Holt [12]. The flow parameters and geometries are described in Table 4.1. *Note: For ease of comparison with previous work, results for configuration A are shown inverted about the cylinder horizontal center-line.*

For each configuration, three grids providing varying degrees of resolution in both the ξ and η directions are utilized. The inflow boundary [AB in Fig. 4.1] is assumed to be a sequence of piecewise smooth spirals bounding the domain of interest. For Config. A, the three grids represent increased concentration throughout the domain while for Config. B, the finest grid concentrates more points only in the region of interest. The cases are denoted A1, A2 and A3 representing the coarsest, medium and finest grids respectively with similar nomenclature for Config. B. In the radial direction the grids are stretched algebraically and exponentially for Configs. A and B respectively. The intermediate grids A2 and B2 are displayed in Fig. 4.2. Some of the salient

Table 4.1: Flow parameters

Config.	D	$Re (\times 10^6)$	M_∞	M'_∞	T_∞	P_∞	T_w	δ	X_{shk}	Y_{shk}
A	3.0	2.06	8.03	5.25	200.8	20.6	530	-12.5	-3.50	-0.52
B	3.0	1.53	8.03	4.76	222.6	18.4	530	15.0	3.26	0.82

Legend: D - Diameter of cylinder (in.) Re - Reynolds number (per foot)
 M_∞ - Upstream Mach Number M'_∞ - Post-impinging shock Mach Number
 T_∞ - Freestream temperature (R) P_∞ - Freestream pressure (lb/f^2)
 T_w - Wall temperature (R) δ - Flow deflection angle (deg.)
 X, Y_{shk} - Ref. location of shock (in.)

points of each grid are presented in Table 4.2. Guidelines for grid resolution are taken from the work of Klopfer and Yee [2] who, for interfering flows, recommend a surface cell Reynolds number (Re_c) of roughly 3 for heat-transfer calculations (fixed-wall temperature) and of the order of 10 for adiabatic wall conditions. They also indicate that heat-transfer rates are not particularly sensitive to the circumferential spacing. The most refined grid for each computation satisfies these criteria.

Table 4.2: Grid details

Config.	Case	$IL \times JL$	$Re_c _{av}$	$\Delta\theta _{min}$	$\Delta\theta _{max}$	$\Delta\theta _{av}$
A	1	71×37	7.6	0.50	3.0	2.13
	2	133×67	3.4	0.50	2.0	1.12
	3	197×99	2.0	0.50	1.0	0.76
B	1	77×43	8.0	0.58	3.0	2.0
	2	151×81	3.4	0.58	1.5	1.0
	3	197×131	0.5	0.29	1.5	0.8

Legend: IL - Points in ξ direction

JL - Points in η direction

Re_c - Surface mesh Reynolds number

$\Delta\theta$ - Angular spacing (deg)

Subscripts: av - average

min, max - minimum, maximum

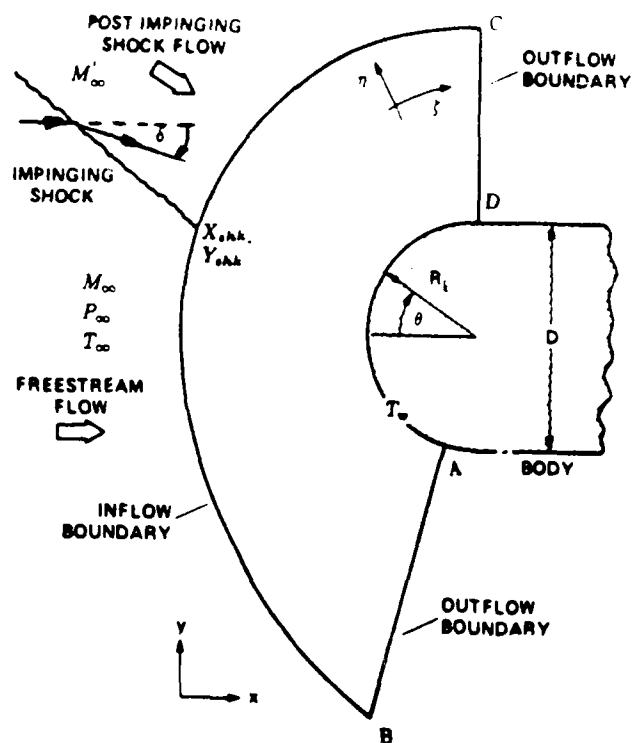


Figure 4.1: Geometry and boundary conditions

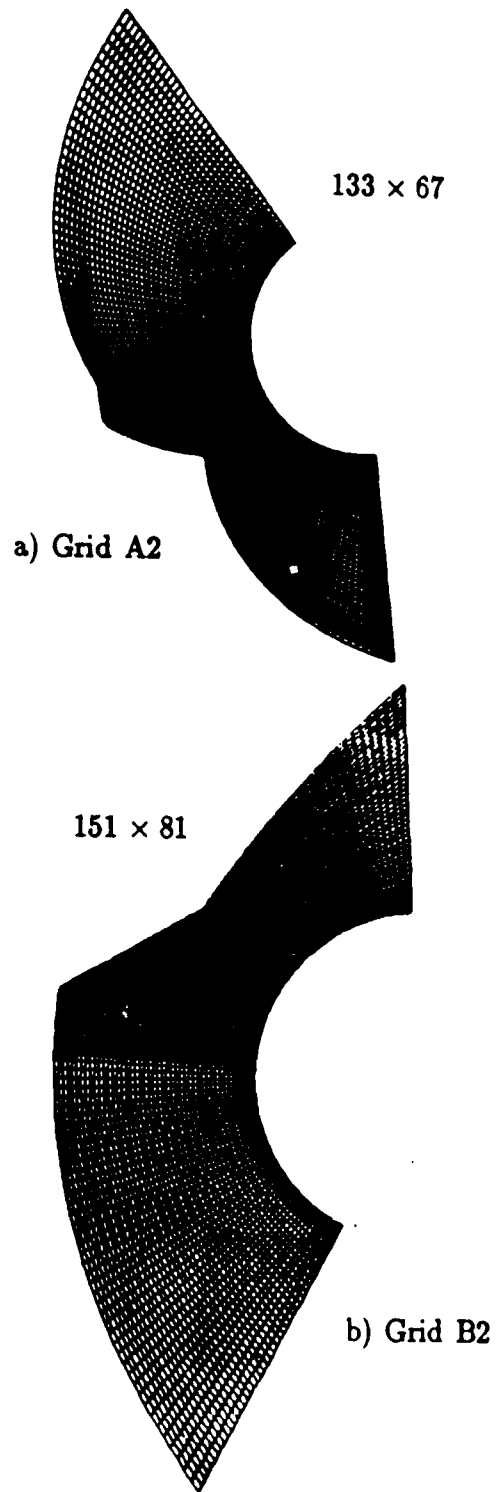


Figure 4.2: Grids for Configs. A and B

5. Boundary Conditions and Numerical Details

With reference to Fig. 4.1, the boundary conditions are as follows:

- "Inflow boundary" [BC]: The flow vector $\{\rho, \rho u, \rho v, \rho e\}$ is specified corresponding to the known values, either upstream or downstream of the impinging shock.
- Solid boundary [AD]: Since this is a solid surface, the velocity vector and the normal pressure gradient are assumed zero and a fixed surface temperature is specified i.e.,

$$\rho \vec{v} = 0; \quad T = T_w; \quad \frac{\partial p}{\partial n} = 0 \quad (5.1)$$

where the subscript w refers to wall conditions. The thermal boundary conditions employed for both configurations are presented in Table 4.1.

- Outflow boundaries [AB,CD]: The flow at these boundaries is assumed predominantly supersonic. The zero gradient extrapolation condition ($\partial/\partial \xi = 0$) is applied.

The boundary conditions for the implicit portion of the algorithm are trivial so far as the freestream is concerned. On the cylinder surface ($j = 1/2$), the viscous and inviscid terms are treated separately to account for the split-flux approach by appropriately modifying the last row of the block tri-diagonal system represented by Eqn. 3.28 after simplification with line relaxation [35].

In all computations described, convergence is determined by monitoring several quantities including maximum and average relative change in the solution vector over a flow development time of roughly three characteristic times (T_c = time required for a particle to traverse the domain at upstream conditions), behavior of the residual and surface quantities – skin friction (τ_w), pressure and heat transfer.

With default compiler vectorization, the code executes at a data processing rate (DPR) of roughly 1.17×10^{-3} secs/(iteration-grid point) on a CRAY-XMP and 1.09×10^{-3} on a CRAY-2.

The algorithm is very stable with permissible CFL numbers (based on inviscid parameters) above 2000 and 5000 for the finer and coarser grids respectively. This permissible CFL is approximately four orders of magnitude larger than that achievable with the explicit MacCormack unsplit scheme.

6. Results and Discussion

6.1 Configuration A

The computed results are first compared with experiment and the computations of Thareja *et al.* [13]. Their results are denoted TSHMP corresponding to the first initials of each of the authors. They computed this configuration with three degrees of mesh refinement with triangular elements. In the following, results from their finest grid, consisting of 5674 triangles and 5792 quadrilaterals, are compared directly with those from the finest grid utilized in this research. The current algorithm and TSHMP differ significantly in approach and methodology. A precise comparison of numerical efficiency or grid sizes employed is not possible since unlike the current method, Thareja *et al.* utilize unstructured adapted grids in their approach.

The heat-transfer comparison is presented in Fig. 6.1 in which are plotted the normalized heat-transfer values against angle along the cylinder (degrees) measured from the noninterfering stagnation line and increasing in the clockwise direction. For normalization purposes, the approach of Thareja *et al.* is followed. Although the experimental noninterfering stagnation heat-transfer value is $61.7 \text{ Btu/ft}^2 - \text{sec}$, they argue that since the theoretical value for peak heat-transfer, obtained with a VSL analysis is 41.43, the difference may be factored out by utilizing the higher (61.7) value to normalize experimental results and the lower value (41.43) for computed values. The results (Fig. 6.1) for the finest grid computed indicate good agreement as regards both peak magnitude and peak location with the values observed by TSHMP with the flux corrected transport (FCT) approach. Peak values are underpredicted by roughly 5% by their FCT approach and by roughly 6% with the current approach. Their basic scheme performs poorest. Away from this stagnation value, the drop in heat-transfer is predicted relatively well by both methods in a region roughly $\pm 10^\circ$ around the stagnation point. Subsequently, all computed values underpredict heat-transfer for negative θ values. It is hypothesized that this is a result

of transition to turbulence. A small bump in heat-transfer values is observed at approximately -30 degrees with the current method. Previous research for the Type *III*⁺ interaction has also displayed similar spatial oscillations downstream of the stagnation point [12].

Fig. 6.2 compares surface pressure values normalized with the noninterfering stagnation pressure. Although the peak pressure location precisely matches the experimental value (to within 0.2 degrees), the value itself is over predicted by roughly 10% on the finest grid. Further, the drop in pressure away from the stagnation point is more rapid with the current method than observed in experiment. For larger negative θ values, significant spatial pressure oscillation is observed qualitatively similar to that observed for the heat-transfer rates. Although TSHMP results do not display these oscillations at least two other methods utilized for shock-shock interactions (van Leer splitting [12] and a TVD scheme [2]) do indeed display similar behavior for Type *III* and Type *IV* flows. For each, the spatial oscillations occur downstream of the shear layer attachment described below. The possibility that these anomalies are slow-decaying transients is currently under investigation. In general however, the comparison of the current method with experiment is good though both algorithms directly compared tend to underpredict pressures away from the interaction.

Fig. 6.3 displays the effect of grid resolution on surface pressure and heat-transfer values. Both peak pressure and heat-transfer values increase and change location slightly with grid refinement. For negative values of θ and away from the stagnation region, the better resolved grids (A2 and A3) display spatial oscillations as observed previously for causes currently unknown. Furthermore, the “bandwidth” of the pressure and heat-transfer profiles also reduces as several features of the flow (see below) are captured with greater clarity in the finer grids. The peak values and locations for both pressure and heat-transfer are presented in Table 6.1. The computations clearly do not display the desirable grid independence and further investigation is warranted.

The ability of the current algorithm to extract the critical flow features is examined by comparison with results from the TSHMP method. For the purposes of brevity, only pressure and

Mach contours are discussed. Fig. 6.4 displays pressure contours for the three computations with the current method and the TSHMP method. The effect of grid resolution is, as anticipated, to provide clearer definition of all flow features. The coarsest grid (Mesh A1) fails to resolve the embedded shock (see schematic of Fig. 1.2) and the high-pressure region near the stagnation point (because of the terminating jet bow shock) where the supersonic jet impinges on the surface is diffuse. The largest pressure rise in the system occurs across the distorted bow shock. Mesh A2 clearly captures all features of the interaction detectable by pressure contours although it is evident from the surface pressure comparisons presented earlier that the required level of accuracy has not yet been reached. The highest resolution examined in this research (Mesh 3) displays the structure of the embedded shock whose orderly deflection by a terminating compression system is clearly exhibited. This compression system is more compact with the current method than with TSHMP. An examination of the Mach contours (Fig. 6.5) reiterates the conclusions derived from the pressure contours in so far as the shock structure is concerned. The shear layer emanating from the intersection point of the impinging shock and the bow shock as also the terminating jet bow shock is not captured at all with the coarsest grid. The shear layer definition emerges with grid refinement. The inviscid shock is captured within at most two grid points in regions where the grid is aligned with the shock and three grid points elsewhere as anticipated from the choice of the unmodified first order Steger-Warming splitting in the vicinity of stronger shock

Table 6.1: Peak pressure and heat-transfer values - Config. A

Case	P/P_o	θ (deg.)	Q/Q_o	θ
A1	5.54	-23.9	5.5	-23.9
A2	8.94	-24.0	7.5	-20.5
A3	9.70	-24.5	13.5	-22.0

waves. The TSHMP method displays crisper bow shock resolution that may be at least partly attributable to grid clustering in their adaptive method. However, the finest grid in the current method displays better resolution of the shear layer structure along the slip and body surfaces. The stand-off distance of the terminating jet bow shock is slightly higher for TSHMP than with the current method.

The streamline pattern on the finest grid is presented in Fig. 6.6. A stagnation line may be clearly defined separating particles flowing over and below the cylinder. A detailed examination of the flow reveals the existence of a small separated region of recirculating flow above the horizontal axis between $\theta \sim 21^\circ$ and $\theta \sim 34^\circ$ and extending over roughly 30 grid points normal to the wall. An examination of the surface pressure plot (Fig. 6.2) reveals a small adverse pressure gradient at $\theta \sim 20^\circ$ and most likely causes separation of the boundary layer developing from the stagnation point. Neither of the coarser grids exhibit this separated region.

The general pattern of the interaction is thus clearly exposed in the current computations and may be classified as as Type IV. The impinging shock intersects the bow shock because of the cylinder at its nearly normal portion. A supersonic jet is formed downstream of the triple point embedded in two shear layers. The size of the supersonic region of the jet may be deduced from Fig. 6.7 which shows the sonic line in the flow. The jet then terminates in a jet bow shock which in turn creates a region of stagnation heating.

6.2 Configuration B

The results obtained with the current scheme for a Type III^+ interaction are compared with the experimental observations of Wieting [39] and computations with the van Leer flux-splitting scheme with and without turbulence reported by Moon and Holt [12]. Their grid is closely comparable to the intermediate grid utilized in this research (Grid B2). As for Config. A, surface quantities are first examined for accuracy. The flow is then analysed for critical features.

Fig. 6.8 exhibits surface pressure values (normalized by the noninterfering stagnation pressure) obtained by all methods. Experimental values remain almost constant until about $\theta \sim 25^\circ$ after which they display a steep rise upto a maximum amplification of roughly 6.2 beyond which they drop again to freestream values. The laminar computation of Moon and Holt (abbreviated *MH* in the figures) overpredicts the peak value by about 100% while results with the current method utilizing a comparable grid (151×81 - B2) displays overprediction of only about 15%. Grid refinement with the current method overpredicts pressure with a maximum amplification of roughly 8.0. The best peak pressure prediction is achieved with the turbulent computation of Moon and Holt where the peak is overpredicted by only less than 0.8 %. All methods successfully reproduce the extent of the pressure amplification region and the angular position of the pressure peak. Both computations of Moon and Holt and the finest grid computed with the current algorithm exhibit significant spatial waviness in the circumferential positions between -10° and 25° .

Fig. 6.9 displays a comparison of heat-transfer rate prediction where the ordinate is the heat-transfer normalized by experimentally observed stagnation heat-transfer values, unlike for Config. A where results from a VSL analysis were utilized. Away from the peak heating region, all laminar computations underpredict heat-transfer leading to the speculation that the boundary layer on either side of the stagnation region rapidly transitions into turbulence. The computations of Moon and Holt (both with and without turbulence) display significant spatial oscillations in the region immediately adjacent to the pressure rise. The peak experimental heat-transfer amplification value is approximately 6.6 occurring at 37.9° . This value is considerably lower than that observed previously for the Type IV interaction. Peak heat-transfer values for both laminar and turbulent computations of Moon and Holt underpredict experiment by approximately 30%. On comparable grids, (151×81 - B2) both the current laminar result and their turbulent computation underpredict the peak heat-transfer although the current method performs marginally better. With further grid refinement (197×131 - Case B3), peak heat-transfer values overpredict

experimental values by 10%. The error in location of peak heat-transfer (roughly 3.0 degrees) may be attributed to small errors in the location of the impinging shock which has previously been observed to be very critical [13]. Peak values and their locations are presented in Table 6.2.

One anomaly evident from Fig. 6.9 is the presence of two peaks, of equal magnitude for case B2 and unequal magnitude for B3. Since the turbulent computation of Moon and Holt also displays this behavior to some extent, this phenomenon was examined in further detail. The peak heat-transfer rates occur at the point where the jet (Type *IV*) or shear layer (Type *III*) impinges the surface of the model and depends not only on the peak pressure generated by the jet but also the width of the jet, the angle at which the jet impinges the surface and whether the jet shear layers are laminar or turbulent [5]. A superposition of Figs. 6.8 and 6.9 indicates that the single pressure peak occurs on the stagnation line which lies between the two heat-transfer peaks. The relative location of the peaks is displayed in Fig. 6.10 which shows flow streamlines near the stagnation point on an enlarged scale. One possible physical explanation hypothesizes significant energy transfer between the flow across the slipstream emanating from the triple point. As a result, the enthalpy of the flow away from the stagnation line is conceivably augmented which might lead to higher heat-transfer at points A and B in Fig. 6.10. Two peaks could be possible therefore depending upon the relative location of the shear layer and the stagnation line. Not much information can be derived from the absence of a pair of peaks for the coarsest grid employed

Table 6.2: Peak pressure and heat-transfer values - Config. B

Case	P/P_o	θ (deg.)	Q/Q_o	θ
B1	5.49	46.0	4.2	43.6
B2	7.69	45.7	5.0	43.9
B3	10.18	45.0	7.7	44.0

(B1 - not shown) since poor resolution smears out most of the flow structure.

It is clear that the above mechanism for creation of the second peak could have a numerical origin. To investigate this possibility, two numerical drawbacks of the current method were examined. First, since the double peaks occur in the vicinity of the stagnation point, the property of flux discontinuity exhibited by the current algorithm was investigated. The eigenvalues (see Eqn. 3.18) were smoothed by adding terms of the type $c \times \frac{\partial \lambda}{\partial \zeta}$ where ζ is appropriately either ξ (for F) or η (for G) and λ is the eigenvalue of the flux vector under consideration. The value of c was fixed at 0.01. The effect of this smoothing on the surface properties and in fact the entire solution was negligible and is not shown. The second numerical possibility concerns the LR correction described in Section 3. As explained there, the effect of the MacCormack and Candler modification was to eliminate a first order damping effect at the expense of a second order artificial pressure gradient whose value was such (Eqn. 3.24) that it achieved significant values only under boundary layer assumptions. The LR correction was proposed as a solution, and in fact, all the computations described with the current method thus far utilized this correction in a linear fashion but only for the surface-normal η direction. A shear layer such as that emanating from a triple-point and impinging on a surface clearly displays significant gradients of the velocities in the circumferential ξ direction and correspondingly a fictitious pressure gradient of unknown magnitude may be expected to exist across it. A small region extending 0.002 radii from the boundary and spanning a region 5° on either side of the stagnation point was therefore identified and a correction similar to the LR correction was applied also in the ξ direction. The results are shown in Fig. 6.11 for both Cases B2 and B3. The anomaly near the stagnation point is eliminated. For the medium grid B2, the maximum heat-transfer increases by about 10% (underpredicts maximum experimental values by 16%) while for the finer grid B3, the effect is much more pronounced with peak heat rates increasing nearly 25% (overpredicting maximum experimental heat-transfer by 45%). The location of the peaks is 2.5° in error. The surface pressure is not significantly influenced and is therefore not shown.

Further comparison with the turbulent computation of Moon and Holt are made by examining the flow structure. The equivalent Grid B2 is utilized for this purpose. Fig. 6.12 displays static pressure contours in the stagnation region. The overall comparison is good. The shock structure is identical (to within one grid point) although the smearing of the shock is modestly greater with the current method since this algorithm reverts to the original Steger Warming formulation at shock waves. The reflected shock manifests as a compression fan near the stagnation point. This fan is larger for the current method.

The Mach contour plots are displayed in Fig. 6.13 on roughly identical scales. The flow is generally classified as a type III^+ since it possesses features representing transition from type III to IV . The impinging shock interacts with the bow shock causing displacement of the latter with the creation of a transmitted shock. A shear layer emanates from the "triple" point. The flow in the shear layer is decelerated as it approaches the surface becoming subsonic with a near normal shock as observed in Fig. 6.14 which displays the sonic line.

Overall, van Leer's splitting provides a sharper representation of the shocks than the current scheme which is essentially a Steger Warming scheme near shock waves. This excessive diffusivity of the Steger Warming scheme was observed previously by Anderson *et al.* [32]. The reflected shock as well as the shear layer emanating from the point of intersection of the reflected shock and the displaced bow shock are clearly resolved with the current algorithm although over more zones than with van Leer's splitting. No over or undershoots in Mach number are observed in the current results.

Flow streamlines obtained with the two methods are displayed in Fig. 6.15. Streams deflected through the distorted bow shock are turned toward the body surface but, unlike the Type IV interaction, do not impinge directly upon the body surface. Moon and Holt indicate that the features separating a Type III^+ flow from a Type III flow are: (i) infant stage of the supersonic jet, (ii) terminating bow shock, and (iii) boundary layer separation. The infant stage of the supersonic (feature (i)) jet is observed in the flow above the stagnation line which first decelerates

through a strong shock (feature (ii)). For this interaction, the shock is nearly perpendicular to the body surface because of the particular angle between the shear layer flow and the body surface. Subsequently, the flow rapidly accelerates to supersonic and may be considered to be the inception of a supersonic jet that would exist if the interaction were Type *IV*. This may happen if, for example, the shear layer angle changed modestly in the direction of the body so as to graze the cylinder surface. Regarding feature (iii), no boundary layer separation was observed, for any of the computations performed for this configuration.

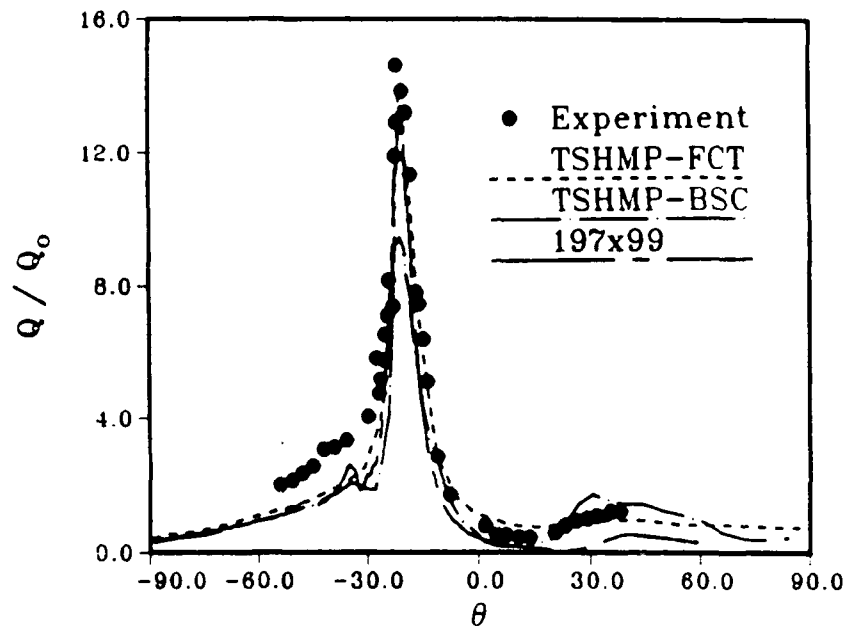


Figure 6.1: Surface heat-transfer comparison - Config. A

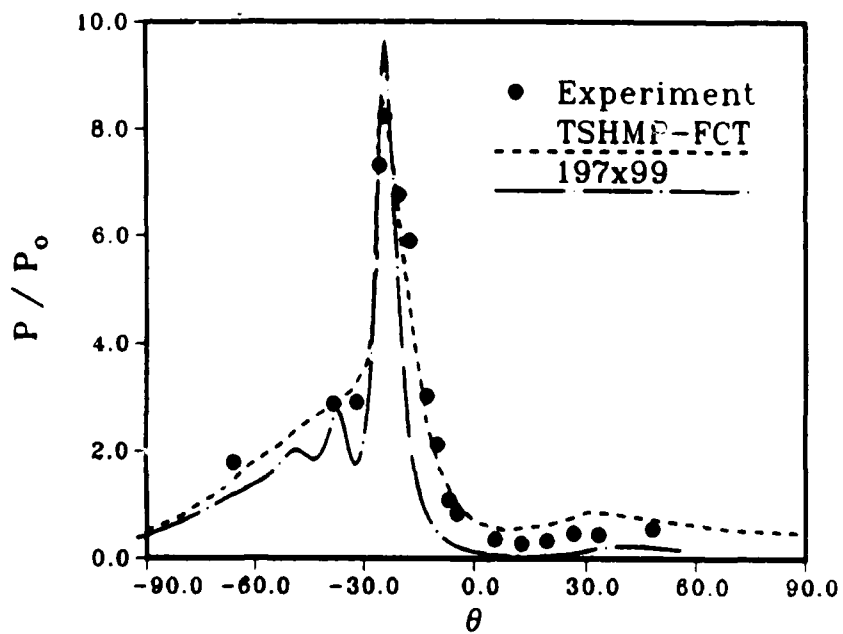
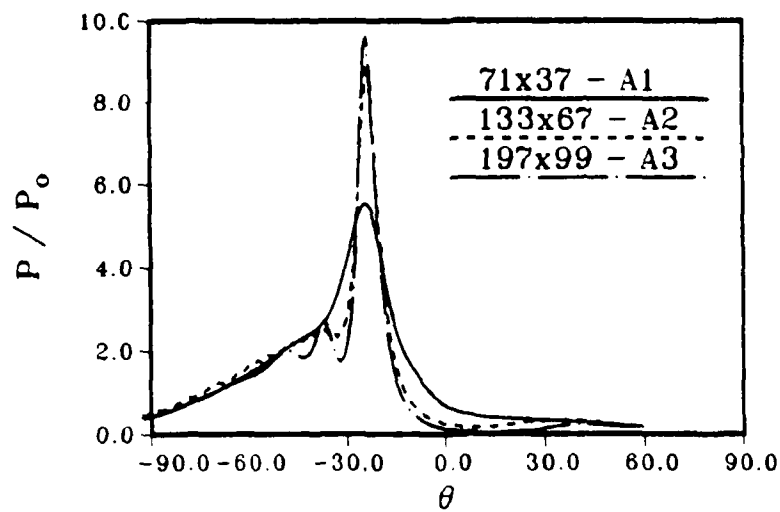
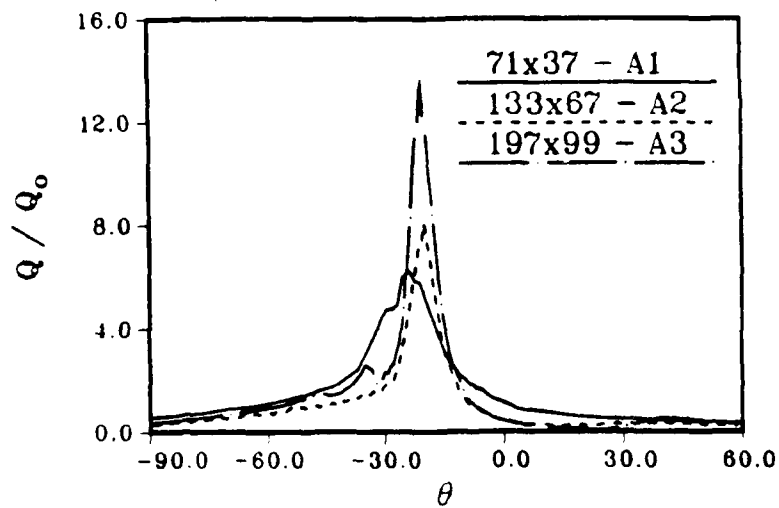


Figure 6.2: Surface pressure comparison - Config. A



(a) Surface Pressure



(b) Surface heat transfer

Figure 6.3: Effect of grid resolution - Config. A

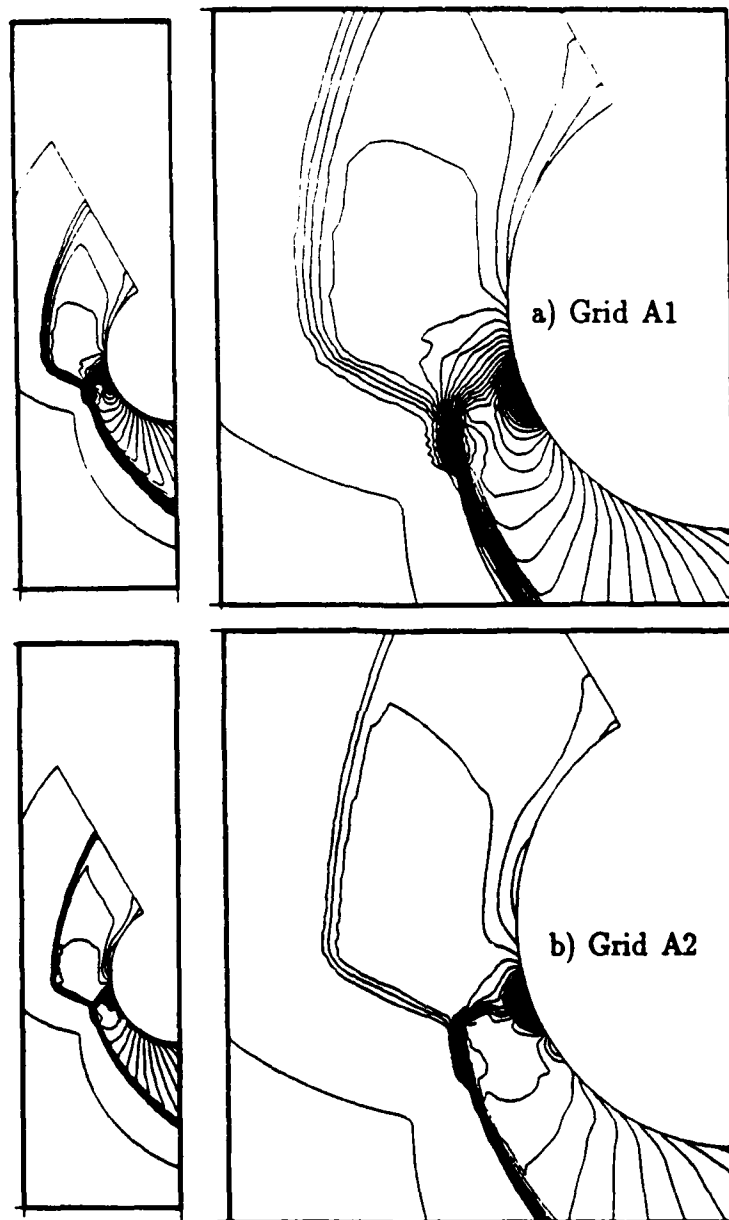


Figure 6.4: Comparison of pressure contours - Config. A (..over)

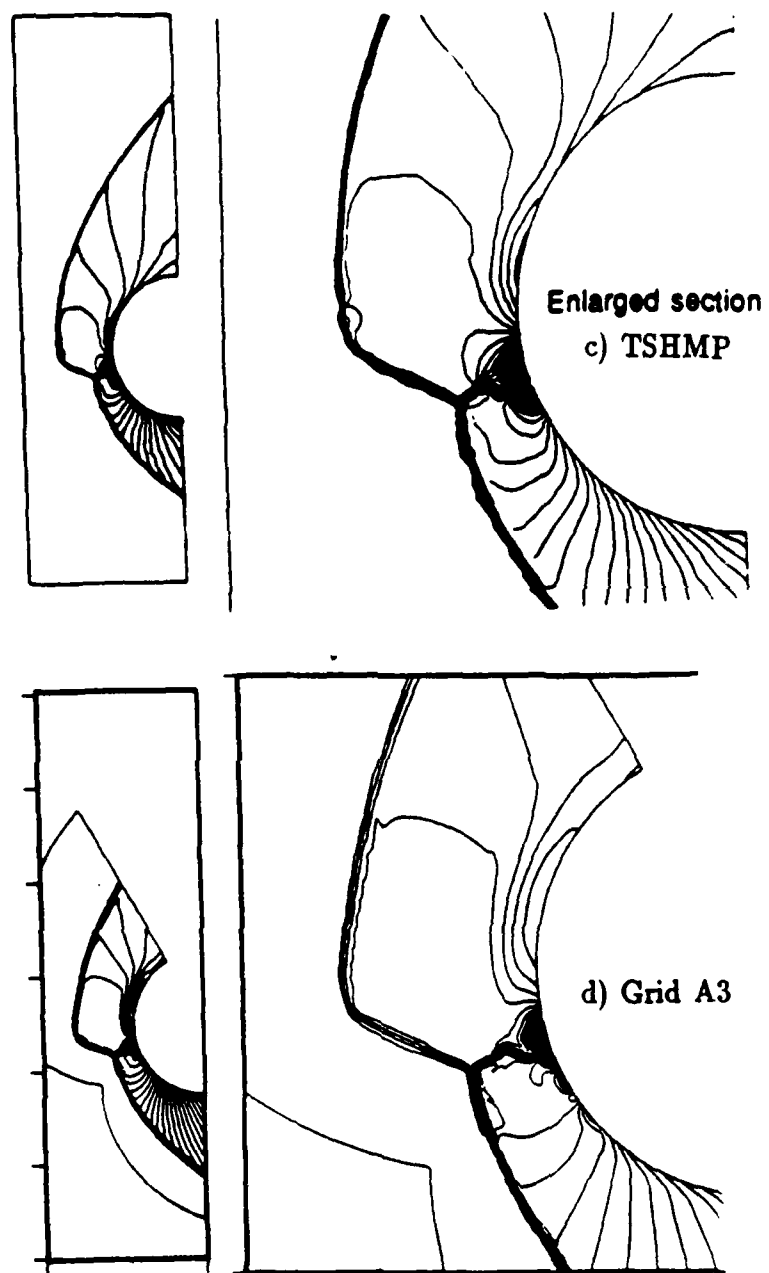


Figure 6.4: Comparison of pressure contours - Config. A (concluded)

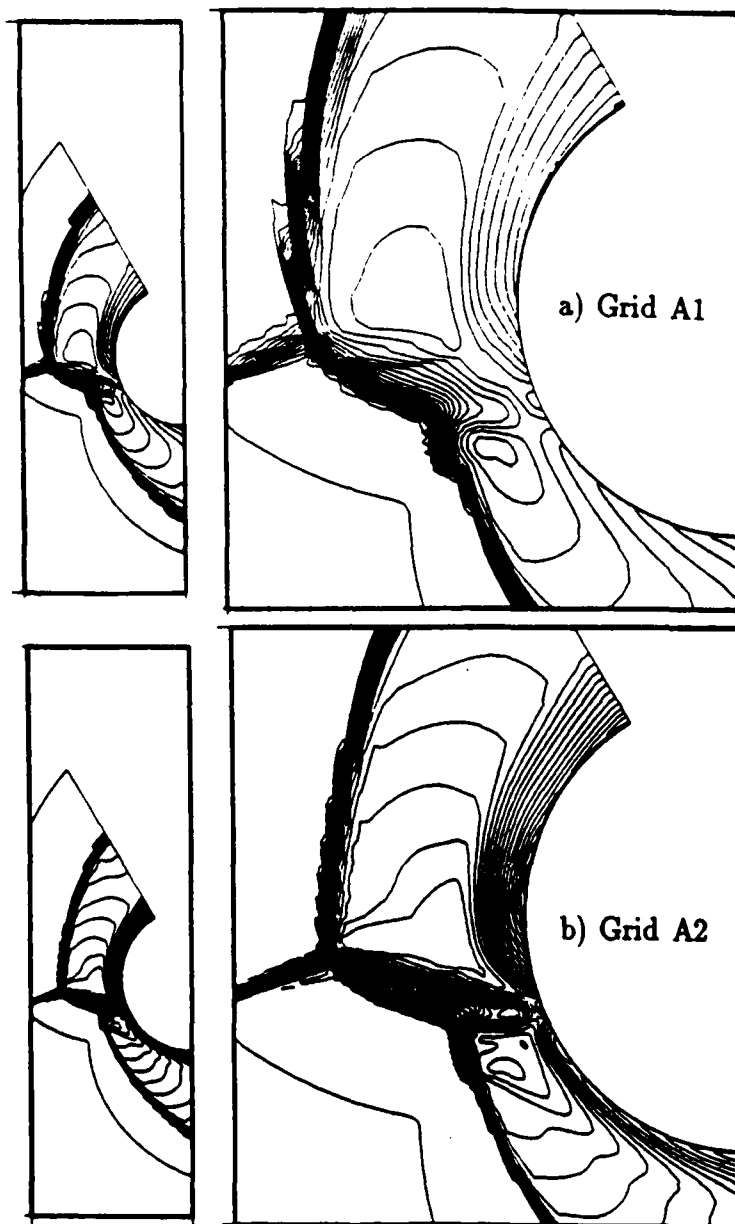


Figure 6.5: Comparison of Mach contours - Config. A (..over)

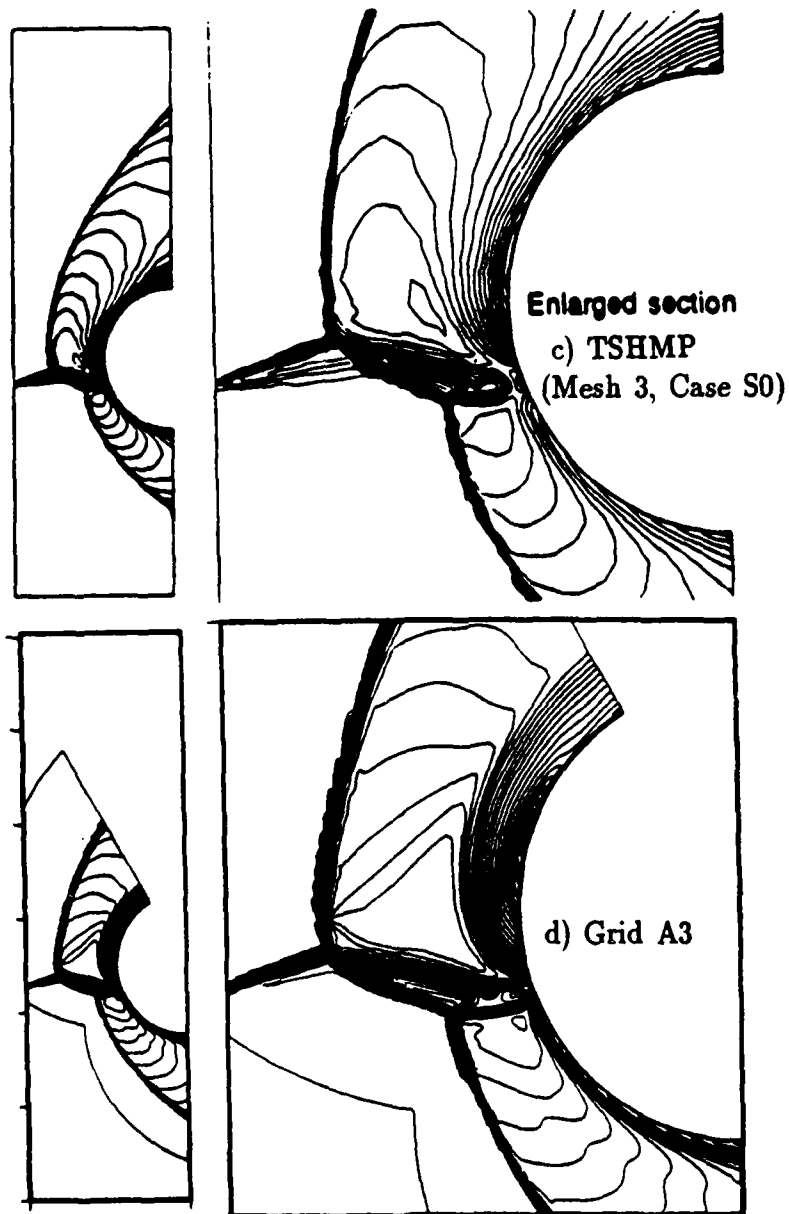


Figure 6.5: Comparison of Mach contours - Config. A (concluded)

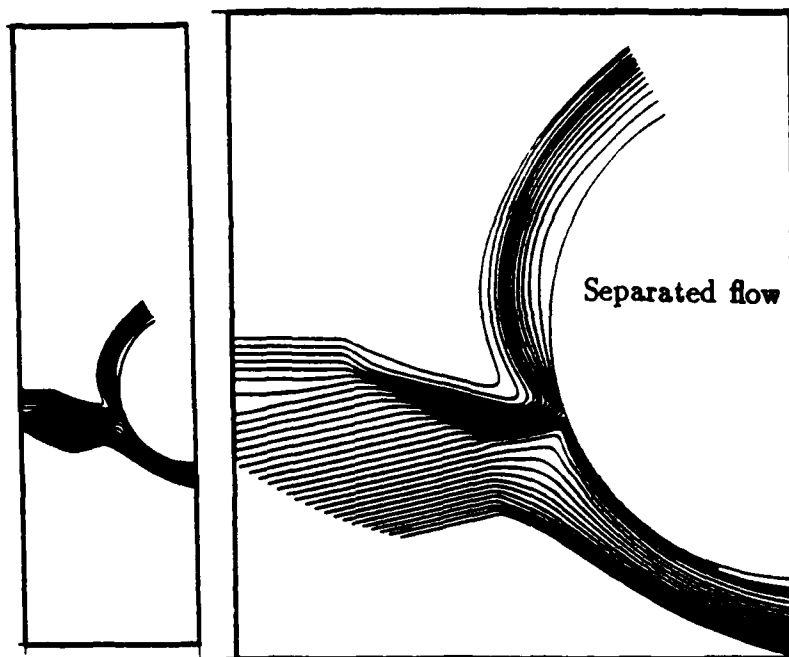


Figure 6.6: Streamlines - Config. A (Grid A3)

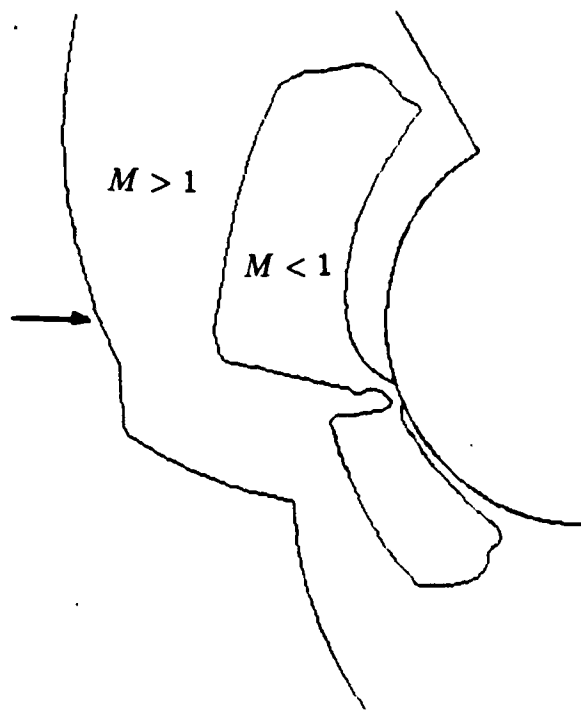


Figure 6.7: Sonic line - Config. A (Grid A3)

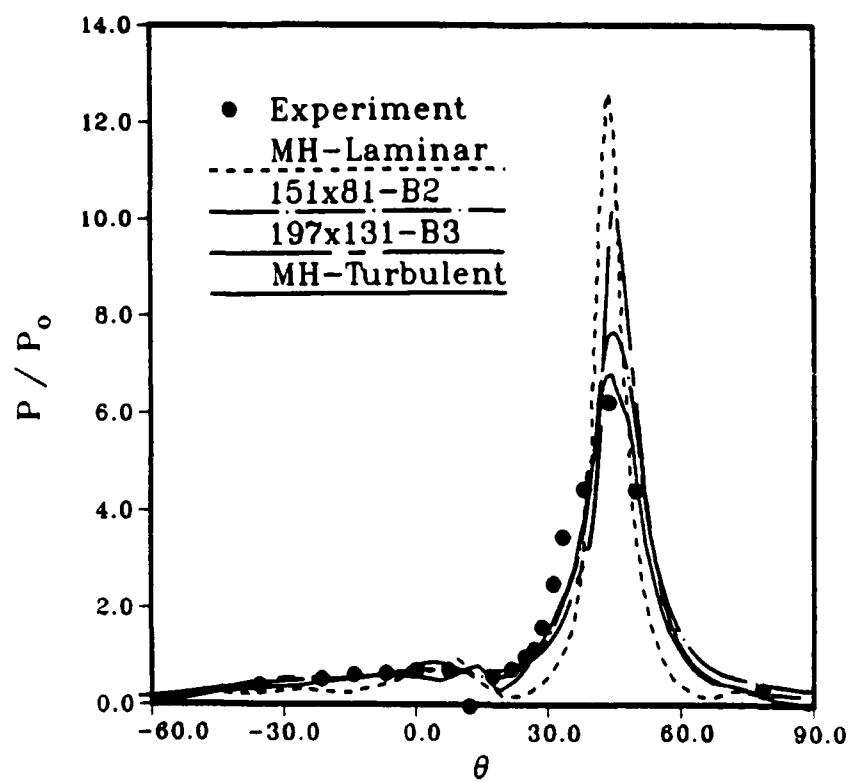


Figure 6.8: Comparison of surface pressure - Config. B

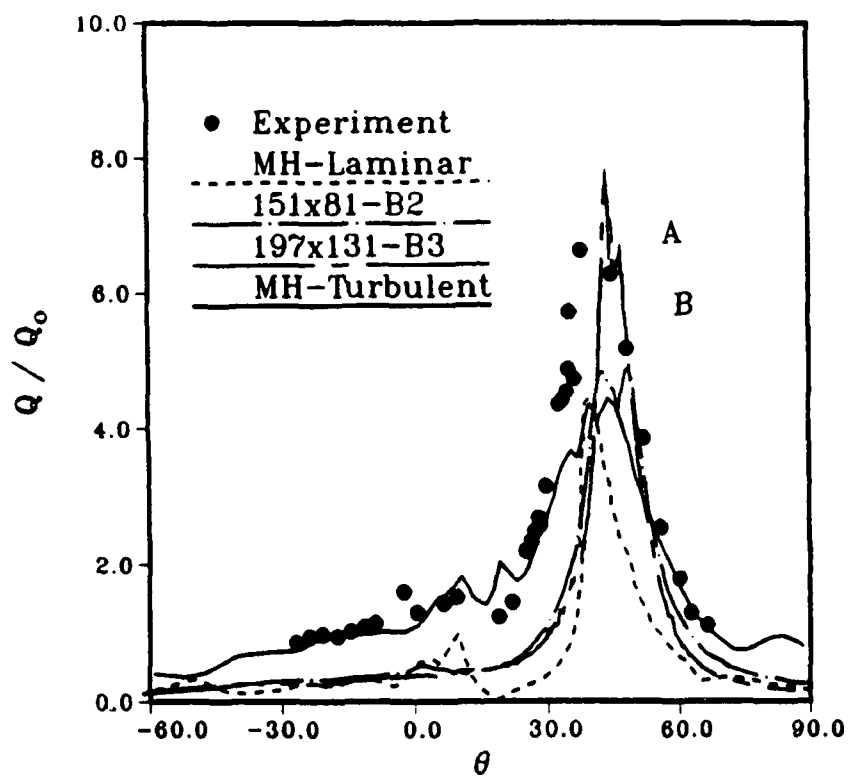


Figure 6.9: Comparison of surface heat-transfer - Config. B

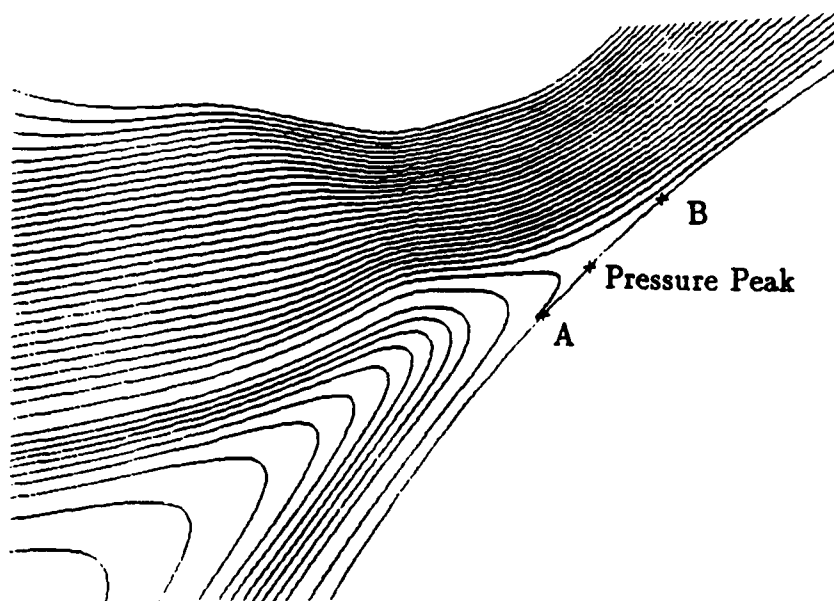


Figure 6.10: Location of pressure and heat-transfer peaks - Config. B2

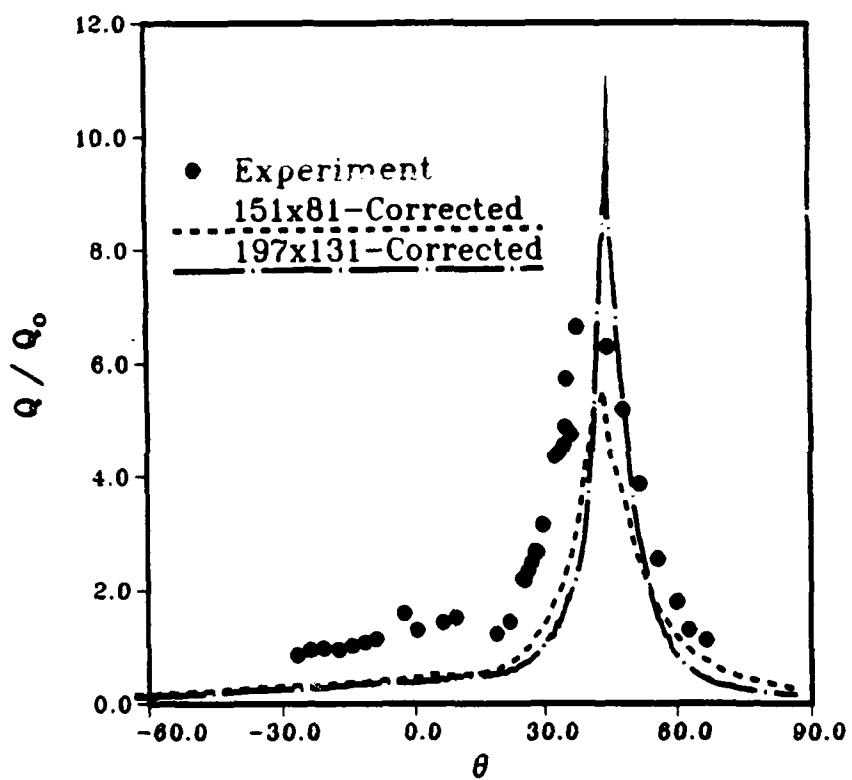


Figure 6.11: Corrected surface heat-transfer - Config. B2

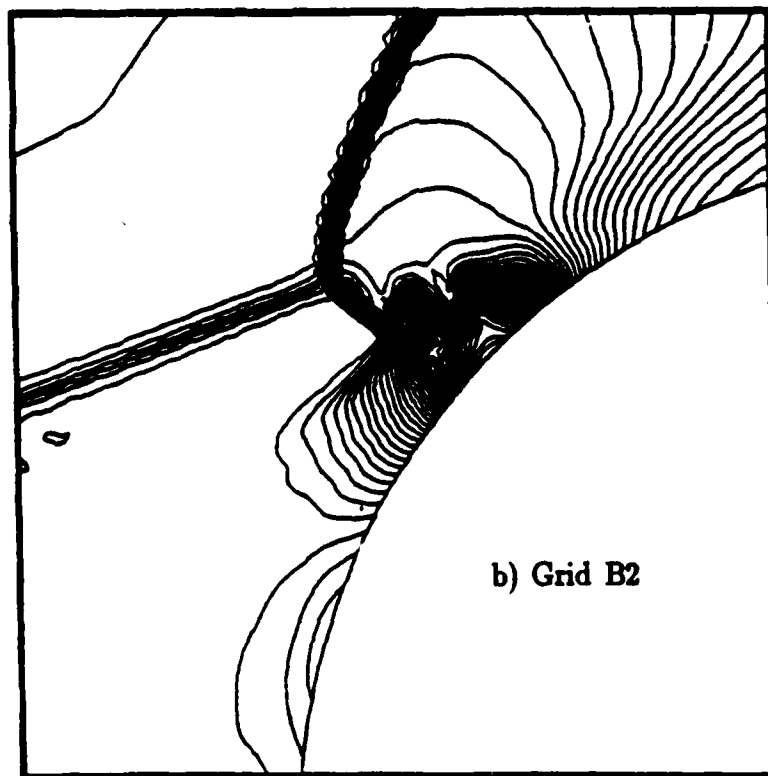
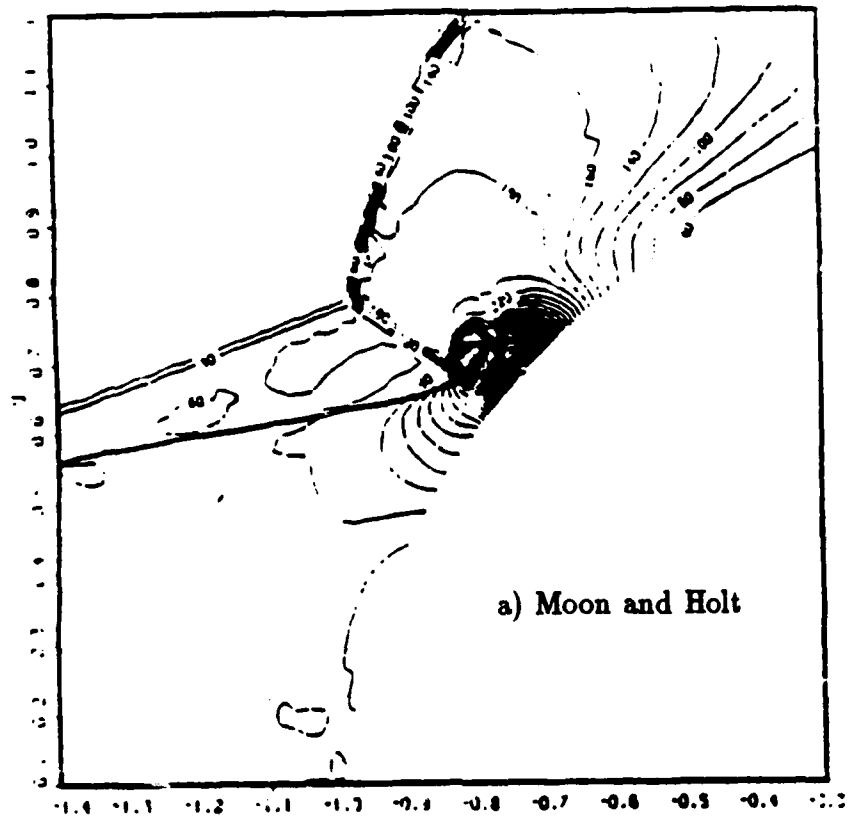


Figure 6.12: Comparison of pressure contours - Config. B

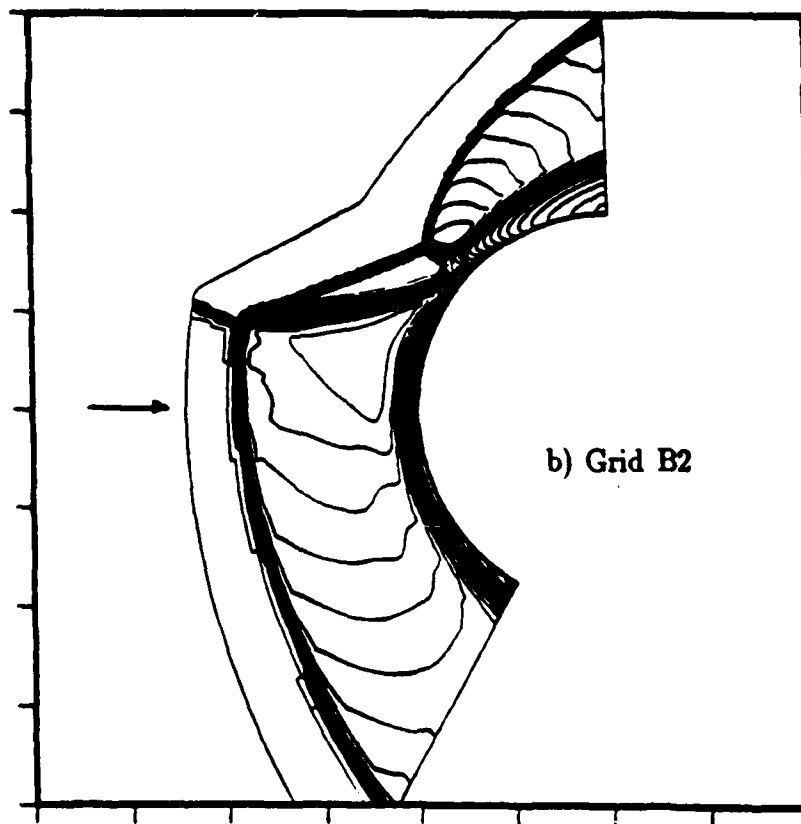
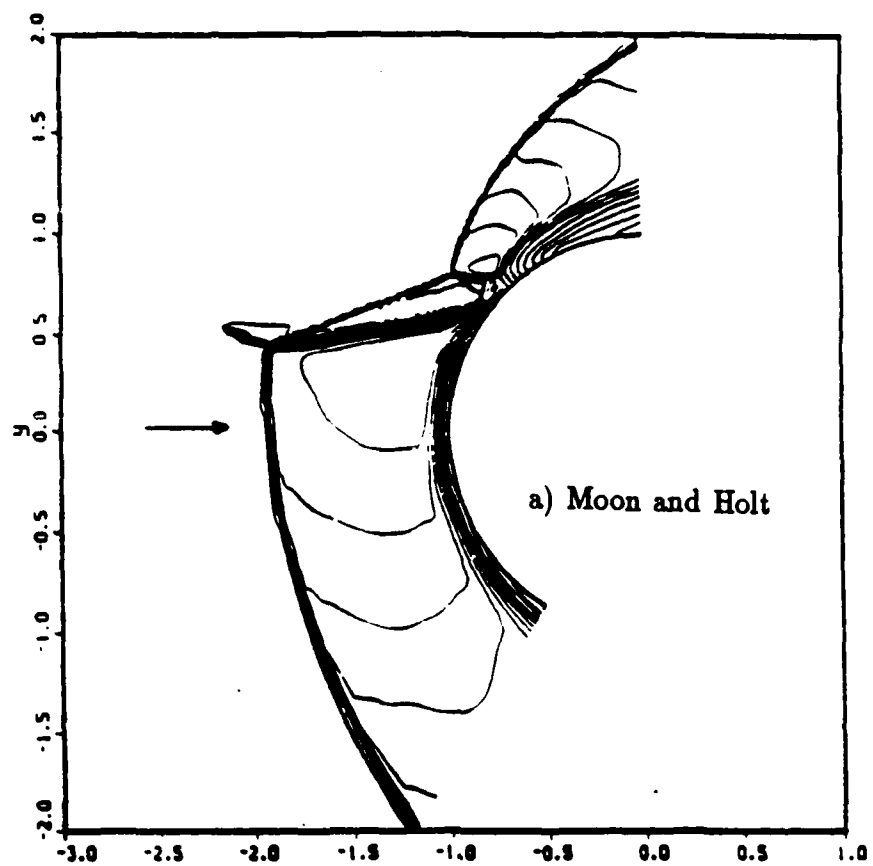


Figure 6.13: Comparison of Mach contours - Config. B

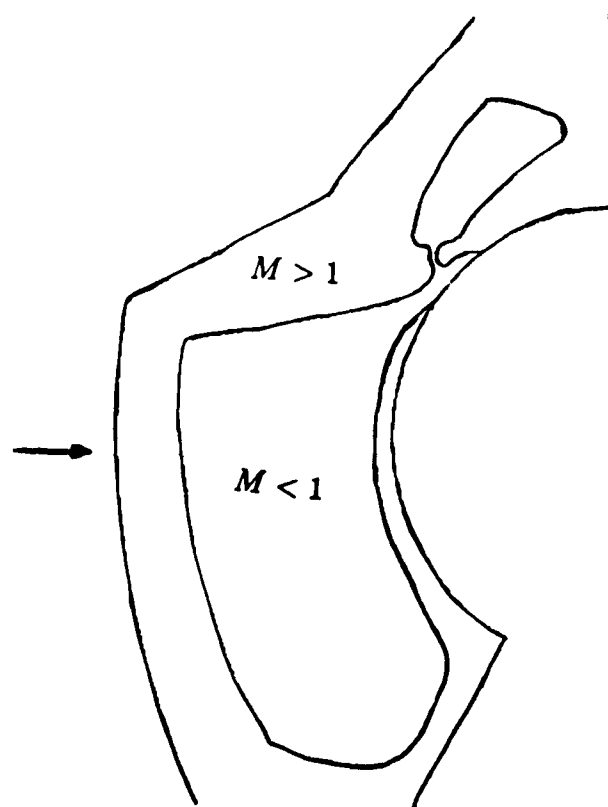
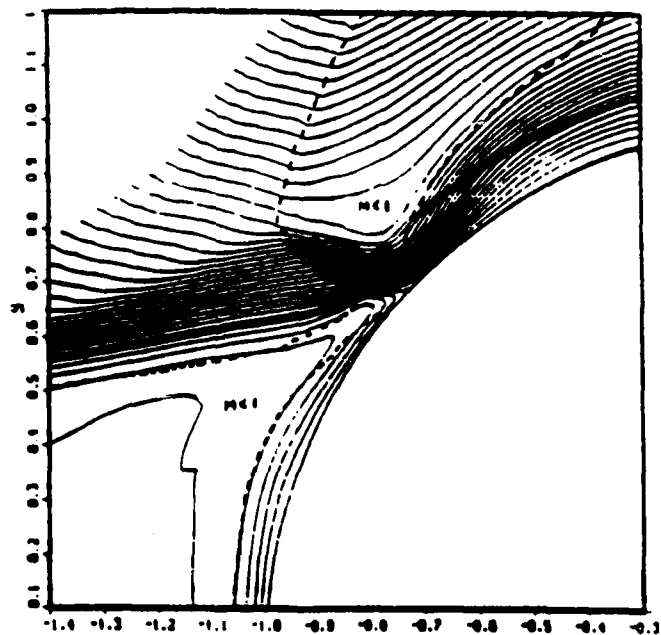
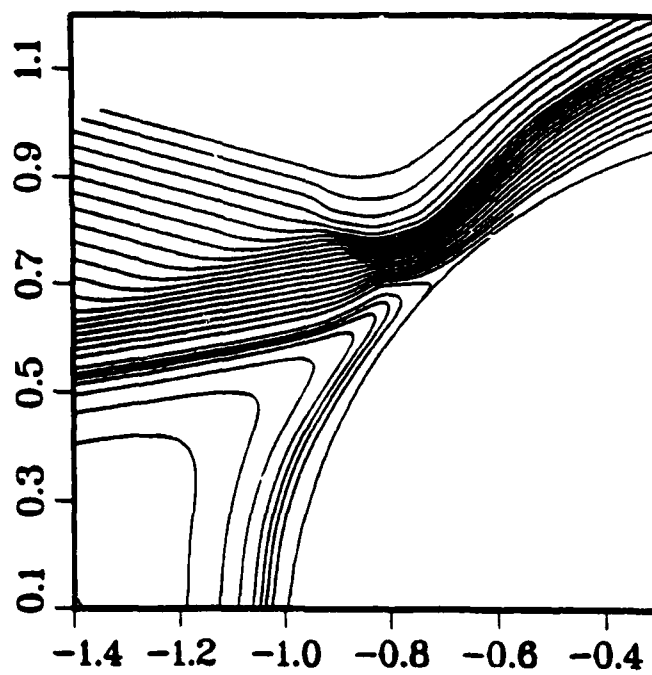


Figure 6.14: Sonic Line - Config. B2



a) Moon and Holt



b) Grid B2

Figure 6.15: Streamline comparison - Config. B

7. Conclusions

Viscous shock-on-shock interactions are examined with a modified Steger Warming scheme displaying low numerical dissipation in boundary layers. For a Type *IV* interaction, peak heat transfer and pressure results are in relatively good agreement with experiment. Modest discrepancies away from the stagnation point, we believe, are due to the existence of boundary layer transition to turbulence which was not modeled in this research. The computed shock and shear layer patterns compare well with those obtained with other methods. A small region of separated flow is observed in the finest grid computed. For a Type *III*⁺ interaction, the algorithm displays spatial heat-transfer oscillations caused most likely by fictitious pressure gradients in the region of peak heating. These gradients are successfully eliminated by appropriate local corrections. Overall, grid refinement leads to overprediction of peak pressures and heat-transfer rates. Thus, on the meshes examined, grid independence is not observed and further investigation is necessary.

8. References

- [1] J.A. White and C.M. Rhie. Numerical Analysis of Peak Heat Transfer Rates for Hypersonic Flow Over a Cowl Leading Edge. *AIAA Paper 87-1895*, 1987.
- [2] G.H. Klopfer and H.C. Yee. Viscous Hypersonic Shock-On-Shock Interaction on Blunt Cowl Lips. *AIAA Paper 88-0233*, 1988.
- [3] Committee on Hypersonic Technology for Military Application. Hypersonic Technology for Military Applications. Technical report, National Academic Press, Washington, D.C, 1989.
- [4] B. Edney. Anomalous Heat Transfer and Pressure Distributions on Blunt Bodies at Hypersonic Speeds in the Presence of an Impinging Shock. Technical Report 115, The Aeronautical Research Institute of Sweden, Stockholm, February 1968.
- [5] A.R. Wieting and M.S. Holden. Experimental Study of Shock Wave Interference Heating on a Cylindrical Leading Edge at Mach 6 and 8. *AIAA Paper 87-1511*, 1987.
- [6] R. Craig and P. Ortwerth. Experimental Study of Shock Impingement on a Blunt Leading Edge with Application to Hypersonic Inlet Design. Technical Report TR-71-10, AFAPL, October 1971.
- [7] M.S. Holden, A.R. Wieting, J.R. Moselle, and C. Glass. Studies of Aerothermal Loads Generated in Regions of Shock/Shock Interaction in Hypersonic Flow. *AIAA Paper 88-0477*, 1986.
- [8] D.J Morris and J.W. Keyes. Computer Programs For Predicting Supersonic and Hypersonic Interference Flow Fields and Heating. Technical Report TM X-2725, NASA, May 1973.
- [9] D.H. Crawford. A Graphical Method for the Investigation of Shock Interference Phenomena. *AIAA Journal*, 11(11):1590-1592, November 1973.

- [10] T.T. Bramlette. Simple Technique for Predicting Type III and Type IV Shock Interference. *AIAA Journal*, 12(8):1151-1152, August 1974.
- [11] J. Tannehill, T. Holst, and J. Rakich. Numerical Computation of Two-Dimensional Viscous Blunt Body Flows with an Impinging Shock. *AIAA Journal*, 14(2), February 1976.
- [12] Y.J. Moon and M. Holt. Interaction of an Oblique Shock Wave with Turbulent Hypersonic Blunt Body Flows. *AIAA Paper 89-0272*, 1989.
- [13] R.R. Thareja, J.R. Stewart, O. Hassan, K. Morgan, and J. Peraire. A Point Implicit Unstructured Grid Solver for the Euler and Navier-Stokes Equations. *International Journal for Numerical Methods in Fluids*, 1989.
- [14] F.D. Hains and J.W. Keyes. Shock Interference Heating in Hypersonic Flows. *AIAA Journal*, 10(11):1441-1447, November 1972.
- [15] I. Beckwith and N. Cohen. Application of Similar Solutions to Calculation of Laminar Heat Transfer on Bodies with Yaw and Large Pressure Gradient in High-Speed Flow. Technical Report TN D-625, NASA, 1961.
- [16] R. MacCormack. The Effect of Viscosity in Hypervelocity Impact Cratering. *AIAA Paper 69-0354*, 1969.
- [17] A. Jameson, W. Schmidt, and E. Turkel. Numerical Solutions of the Euler Equations by a Finite Volume Method Using Runge-Kutta Time Stepping Schemes. *AIAA Paper 81-1259*, 1981.
- [18] H.C. Yee, G.H. Klopfer, and J.-L. Montagne. High-Resolution Shock-Capturing Schemes for Inviscid and Viscous Hypersonic Flows. Technical Report 100097, NASA - Ames Research Center, Moffet Field, California, April 1988.

- [19] J.L. Steger and R.F. Warming. Flux Vector Splitting of the Inviscid Gasdynamic Equations with Application to Finite Difference Methods. *Journal of Computational Physics*, 40(2):263-293, April 1981.
- [20] B. van Leer. Flux-Vector Splitting For the Euler Equations. Technical Report 82-30, ICASE, September 1982.
- [21] R.F. Warming and R.M. Beam. Upwind Second-Order Difference Schemes and Applications in Aerodynamic Flows. *AIAA Journal*, 14(9):1241-1249, September 1976.
- [22] R.F. Warming and R.M. Beam. On the Construction and Application of Implicit Factored Schemes for Conservation Laws. In *Symposium on CFD*. SIAM-AMS, 1978.
- [23] H.C. Yee. A Class of High-Resolution Explicit and Implicit Shock-capturing methods. Technical Report TM 101088, NASA, February 1989.
- [24] C-J. Woan and S.R. Chakravarthy. Transonic Euler Calculations of a Wing-Body Configuration Using a High-Accuracy TVD Scheme. *AIAA Paper 88-2547-CP*, 1988.
- [25] P. Buelow. Comparison of TVD Schemes Applied to the Navier-Stokes Equations. *AIAA Paper 89-0847*, 1989.
- [26] W.K. Anderson, J.L. Thomas, and D.L. Whitfield. Multigrid Acceleration of the Flux Split Euler Equations. *AIAA Paper 86-0274*, 1986.
- [27] J.L. Thomas and R.W. Walters. Upwind Relaxation Algorithms for the Navier Stokes Equations. *AIAA Paper 85-1501*, 1985.
- [28] J.L. Thomas, S.L. Taylor, and W.K. Anderson. Navier-Stokes Computations of Vortical Flows Over Low Aspect Ratio Wings. *AIAA Paper 87-0207*, 1987.

- [29] P.G. Buning and J.L. Steger. Solution of the Two-Dimensional Euler Equations with Generalized Coordinate Transformation Using Flux Vector Splitting. *AIAA Paper 82-0971*, 1982.
- [30] R.W. MacCormack and G.V. Candler. The Solution of the Navier-Stokes Equations with Gauss-Seidel Line Relaxation. *Symposium in Honor of G. Moretti's 70th Birthday*, 1987.
- [31] G.V. Candler and R.W. MacCormack. The Computation of Hypersonic Ionized Flows in Chemical and Thermal Nonequilibrium. *AIAA Paper 88-0511*, 1988.
- [32] W.K. Anderson, J.L. Thomas, and B. van Leer. A Comparison of Finite Volume Flux Vector Splittings for the Euler Equations. *AIAA Paper 85-0122*, 1985.
- [33] S.T. Zalesak. Fully Multidimensional Flux Corrected Transport Algorithm for Fluids. *Journal of Computational Physics*, 31:335-362, 1979.
- [34] B. van Leer, J.L. Thomas, P.L. Roe, and R.W. Newsome. A Comparison of Numerical Flux Formulas for the Euler and Navier-Stokes Equations. *AIAA Paper 87-1104*, 1987.
- [35] G.V. Candler. *The Computation of Weakly Ionized Hypersonic Flows In Thermo-Chemical Nonequilibrium*. PhD thesis, Stanford University, California, 1988.
- [36] R. MacCormack. Current Status of Numerical Solutions of the Navier-Stokes Equations. *AIAA Paper 85-0032*, 1985.
- [37] M-S. Liou and B. van Leer. Choice of Implicit and Explicit Operators For the Upwind Differencing Method. *AIAA Paper 88-0624*, 1988.
- [38] J.L. Thomas, B. van Leer, and R.W. Walters. Implicit Flux-Split Schemes for the Euler Equations. *AIAA Paper 85-1680*, 1985.
- [39] A.R. Wieting. Experimental Study of Shock Wave Interference Heating on a Cylindrical Leading Edge. Technical Report 100484, NASA, May 1987.

Nomenclature

B	Jacobian of flux vector G with respect to \bar{U}
c	generic constant
C_p	specific heat at constant pressure
C_v	specific heat at constant volume
D	diameter
DPR	Data Processing Rate
e	total energy
e_i	internal energy
F, \bar{F}, G, \bar{G}	flux vectors
FCT	Flux Corrected Transport Method
IL, JL	Points in ξ and η directions respectively
J	Jacobian of transformation
LR	Last Row correction
M	Mach number
n	iteration number
P, p	pressure
Q	heat transfer component; similarity transformation matrix
R	Gas constant for air
Re	Reynolds number
t	time
T	Temperature; time
$TSHMP$	Thareja, Stewart, Hassan, Morgan and Peraire

TVD Total Variation Diminishing Schemes

u Cartesian velocity in x direction

\bar{U} solution vector

U contravariant velocity vector

v Cartesian velocity in y direction

\vec{v} Cartesian velocity vector

V contravariant velocity vector

VSL Viscous Shear Layer Analysis

x, y physical coordinates

α kinetic energy

δ change; angle

Δ switch threshold; change

∂ partial derivative

η transformed coordinate

γ ratio of specific heats

λ second coefficient of viscosity

μ molecular viscosity

ϕ constant in limiter function

ρ density

$\bar{\tau}$ Cartesian stress tensor

θ angle

ξ transformed variable

Subscripts

av average

c characteristic

i component i ; internal

j component j ; face j

max maximum value

min minimum value

w wall

x, y Cartesian coordinate directions

η derivative with respect to η

ξ derivative with respect to ξ

∞ freestream value